Synchrotron X-ray Topography Analysis of Dislocation Line Directions in 4H-SiC Single Crystals

A Thesis Presented

by

Jianing Yan

to

The Graduate School

in Partial Fulfillment of the

Requirements

for the Degree of

Master of Science

in

Materials Science and Engineering

Stony Brook University

May 2016

Stony Brook University

The Graduate School

Jianing Yan

We, the thesis committee for the above candidate for the

Master of Science degree, hereby recommend

acceptance of this thesis.

Michael Dudley
Professor, Department of Materials Science and Engineering

Balaji Raghothamachar
Research Professor, Department of Materials Science and Engineering

T.A. Venkatesh
Associate Professor, Department of Materials Science and Engineering

This thesis is accepted by the Graduate School

Charles Taber
Dean of the Graduate School

Abstract of the Thesis

Synchrotron X-ray Topography Analysis of Dislocation Line Directions in 4H-SiC Single Crystals

by

Jianing Yan

Master of Science

in

Materials Science and Engineering

Stony Brook University

2016

This thesis presents a Synchrotron White Beam X-ray Topography study of dislocations in 4H-SiC single crystals. Basic introduction is given including the crystal structure and atomic arrangement, crystal growth techniques, and the dislocation types. The commonly observed dislocations, including Micropipes (MPs), Basal Plane Dislocations (BPDs), Threading Screw Dislocations (TSDs), Threading Edge Dislocations (TEDs), Threading Mixed Dislocations (TMDs), in 4H-SiC single crystals have been reviewed. Since the extensive application of SiC for power devices is limited by the presence of these dislocations, the minimization, and eventually elimination of these dislocations, have been a major impetus in both research and commercial areas. Therefore, the importance of understanding the formation and multiplication mechanisms of dislocations is highlighted.

An effective way to obtain detailed information on dislocations is line direction analysis in combination with Burgers vector determination to enable deducing the origins and glide orientations of various dislocations. To facilitate this, a method which can trace back the directions of the dislocations inside real crystals from two different dislocation X-ray topographic images, is developed and applied. The basic concept combines the crystal structure, rotation parameters and any two line-directions recorded on the X-ray film to determine the actual dislocation line direction in the real crystal. The hexagonal structure of 4H-SiC has been used to develop a computer program using JavaScript to perform this calculation. But the developed program can be easily modified to analyze dislocation line directions in any crystal structure. Application of the program using information from X-ray topographic images quickly produces quantitative results and also provides a graphical visualization of the 3D positions of dislocation lines inside 4H-SiC crystals. Combined with Burgers vector data allows an effective way to analyze the formation mechanism and multiplication tendency of dislocations in crystals. Examples of this implementation are provided to demonstrate the significance of this procedure.

Table of Contents

Abstract of the Thesis .... **iii**

Table of Contents .... **iv**

List of Figures .... **v**

List of Tables .... **vii**

List of Abbreviations .... **viii**

List of Symbols .... **ix**

Acknowledgments .... **xi**

1. Introduction **1**
- **1.1 Background of Silicon Carbide (SiC)** **1**
- **1.2 Crystal Growth Technique for SiC** **3**
- **1.3 Defect Structure and Reduction in SiC** **5**
  - 1.3.1 Micropipe (MP) 6
  - 1.3.2 Threading Screw Dislocation (TSD) 8
  - 1.3.3 Threading Edge Dislocation (TED) 9
  - 1.3.4 Basal Plane Dislocation (BPD) 11

2. Characterization Technique **13**
- **2.1 Synchrotron X-ray Topography (SXRT)** **13**
- **2.2 Geometries for Diffraction Images** **15**

3. Dislocation Line Direction Analysis and Simulation in 4H-SiC **17**
- **3.1 Outline** **17**
- **3.2 Calculation Procedure** **18**
- **3.3 Experimental and results** **29**

4. Summary **36**
- **Conclusions** **36**
- **Future Work** **36**

Appendix: Code of Program **40**

List of Figures

Figure 1-1 Stacking sequence of 3C-, 4H- and 6H-SiC 2
Figure 1-2 Schematic of the PVT method [9] 3
Figure 1-3 Schematic drawings of the most commonly used CVD reactors. [11,13] 4
Figure 1-4 Evolution of Si and SiC wafer technologies..5
Figure 1-5 (from left to right) A straight BPD in (0001) basal plane; A TSD along [0001] line direction with n [0001] Burgers vector; A TED along [0001] line direction with Burgers vector on basal plane 6
Figure 1-6 (a) Back reflection image for 6H-SiC wafer contained MPs and TSDs; (b) and (c) show an enlarged MP and accordingly simulation result [21]..7
Figure 1-7 Reduction of MP densities in Dow Corning 76 mm and 100 mm 4H-SiC wafers [24] 7
Figure 1-8 TSD density vs breakdown voltage in 4H-SiC diode (2000 year) [26]........................8
Figure 1-9 TSDs reduction trend in SiC epilayer and substrate from 2002-2016..........................8
Figure 1-10 TEDs reduction trend in SiC epilayer and substrate from 2002-2016........................9
Figure 1-11 (d)- (j) Formation mechanism of pairs of IDs and half-loop arrays. [35] 10
Figure 1-12 BPDs reduction trend in SiC epilayer and substrate from 2002-2016......................11
Figure 1-13 (a) Synchrotron X-ray image recorded from a 4H-SiC wafer; (b) The loops produced by the Hopping Frank-Read mechanism; (c) Schematic cross-sectional view of the process; (d) Synchrotron X-ray image confirming the existence of the double deflection process between TED and BPD segment [39] 12
Figure 2-1 (a) Synchrotron White Beam X-ray Topography (SWBXRT); (b) Synchrotron Monochromatic X-ray Topography (SMBXRT) 13
Figure 2-2 Location of Laue spots on (a) Transmission method; (b) Back-reflection method. (C=Crystal, F= Film)...14
Figure 2-3 (a) Transmission geometry; (b) Grazing geometry..15
Figure 2-4 Transmission image for a 4H-SiC wafer (area size:1.5mm x 3mm) 15
Figure 2-5 Wafer template with selected square regions and the corresponding grazing image in one region 16
Figure 3-1 Flowchart of program for a given crystal structure 17
Figure 3-2 Schematic illustrate the principle of finding the real dislocation line direction in the crystal...18
Figure 3-3 Diffraction vector determination 19
Figure 3-4 Rhombohedral system showing (111) plane mapped to a Cartesian system 21
Figure 3-5 Orthorhombic system showing (111) plane 23
Figure 3-6 Cartesian Coordinate system used during experiments 24
Figure 3-7 Matrix transformation and rotation...25
Figure 3-8 A sketch showing a plane in the hexagonal coordinate system.................................26
Figure 3-9 A sketch showing rotation around z-axial rotate (+)16° 27
Figure 3-10 The way to measure the angle between dislocation direction and reference direction 28
Figure 3-11 X-ray topographs recorded from axial SiC wafer within particular dislocation line of interest (L_1 and L_2)..29
Figure 3-12 (a) The simulation result of dislocation line direction; (b) Visualized line direction in real crystal...31

Figure 3-13 (a) 4H-SiC axial slice showing a certain area for axial wafer of LA; (b)-(f) The chosen area with different diffraction vectors: (1-101), (1-10-1), (-1100), (0004) and (11-20) 32
Figure 3-14 Threading mixed dislocation slide on plane (1-212) 34
Figure 3-15 A sketch showing a dislocation glide on the pyramidal plane (-211-2)....35

List of Tables

Table 1-1Physical and electronic properties of SiC compared to other commercial semiconductor materials..........1
Table 1-2 Key parameters of 4H-, 6H- and 3C SiC..........2
Table 1-3 Configurations of various types of dislocations...........6
Table 3-1 Values of g. b for TDs..........33

List of Abbreviations

SiC	Silicon Carbide
GaN	Gallium Nitride
WBG	Wide Band-gap
PVT	Physical Vapor Transport
CVD	Chemical Vapor Deposition
BPD	Basal Plane Dislocation
TD	Threading Dislocation
TSD	Threading Screw Dislocation
TED	Threading Edge Dislocation
TMD	Threading Mixed Dislocation
MP	Micropipe
ID	Interfacial Dislocation
HLA	Half-loop Arrays
SXRT	Synchrotron X-Ray Topography
SWBXRT	Synchrotron White Beam X-Ray Topography
SMBXRT	Synchrotron Monochromatic X-Ray Topography

List of Symbols

$\mathbf{g_1}$	Normal of diffraction plane, (h_1, k_1, l_1)
$\mathbf{g_2}$	Normal of diffraction plane, (h_1, k_1, l_2)
$\mathbf{n_1}$	Normal of plane defined by $\mathbf{l_1}$ and $\mathbf{S_{h1}}$
$\mathbf{n_2}$	Normal of plane defined by $\mathbf{l_1}$ and $\mathbf{S_{h2}}$
$\mathbf{S_{h1}}$	Diffraction vector defined by the incident beam direction $\mathbf{S_0}$ and the normal od the plane $(h_1\ k_1\ l_1)$, $\mathbf{g_1}$
$\mathbf{S_{h2}}$	Diffraction vector defined by the incident beam direction $\mathbf{S_0}$ and the normal od the plane $(h_2\ k_2\ l_2)$, $\mathbf{g_2}$
$\mathbf{S_0}$	Incident beam direction
$\mathbf{l_1}$	Dislocation line direction on image $h_1\ k_1\ l_1$
$\mathbf{l_2}$	Dislocation line direction on image $h_2\ k_2\ l_2$
L	Dislocation line direction in the crystal expressed in terms of orthogonal system
a, b , c,	Unit vector of the crystal lattice cell
a, b , c,	Lattice parameter of the unit cell. i.e. magnitude of the crystal lattice vectors
α	Angle between **b** and **c**
β	Angle between **a** and **c**
γ	Angle between **a** and **b**
a*, b*, c*	Reciprocal lattice vectors

a*, b*, c*	Magnitude of reciprocal lattice vectors
V	volume of the crystal unit cell in real space
(h k l)	Miller index in crystal system
(H K L)	Plane index in orthogonal system
G	Matric tense
G^{-1}	Inverse matrix of G
|G|	The determinant of G
$\mathbf{g_x}$, $\mathbf{g_y}$, $\mathbf{g_z}$	Three crystal component of vector **g**
x, y, z	3 axe corresponding to **a, b, c** respectively in the crystal system
X, Y, Z	3 Cartesian axes
θ	Rotation angle

Acknowledgments

First I would like to give my sincere acknowledgement to professor Michael Dudley, my research advisor, who providing me the cherish opportunity to do research in the field of crystal growth and characterization. I could not learn much without his patience, encouragement, and valuable guidance. His wide knowledge and professional attitude toward research have always been providing an excellent basis for my study.

Then I own professor Balaji Raghothamachar for his guidance and instruction both in theory study and experiment. Without his understanding and patience in research, I would never finish this study.

Thank professor T.A.Venkatesh for his guidance and being one my thesis committee.

I also would like to thank my colleagues - Jianqiu, Yang Yu, Yannick. Thanks for their help and encouragement during research and everyday life.

Thank my parents, my boyfriend Cong who are always there for me and supporting me to finish my master study.

1. Introduction

1.1 Background of Silicon Carbide (SiC)

Improving performance, reducing production cost and diminishing packaging size are three important development aspects in semiconductor industry. As people concentrate more on environmental friendly and clean energy sources these years, market demand is increasing for power devices that will approach low-loss, high power density, and high-efficiency power conversion. The qualifications and optimized characteristics of power components, obviously, contribute to the improvements of power products. For example, high blocking voltage, fast switching speed, low reverse leakage current even in high-temperature region, high saturated electron drift limits, and high thermal conductivity could be measurements of advanced performance. As conventional semiconductors such as Silicon power components access their theoretical limits, wide band-gap (WBG) semiconductor materials, Silicon Carbide (SiC) and Gallium Nitride (GaN) for example, have been considered as desirable semiconductors for dramatically improving those parameters listed above. [1] Table 1-1 shows a comparison between SiC and other commercial semiconductor materials.

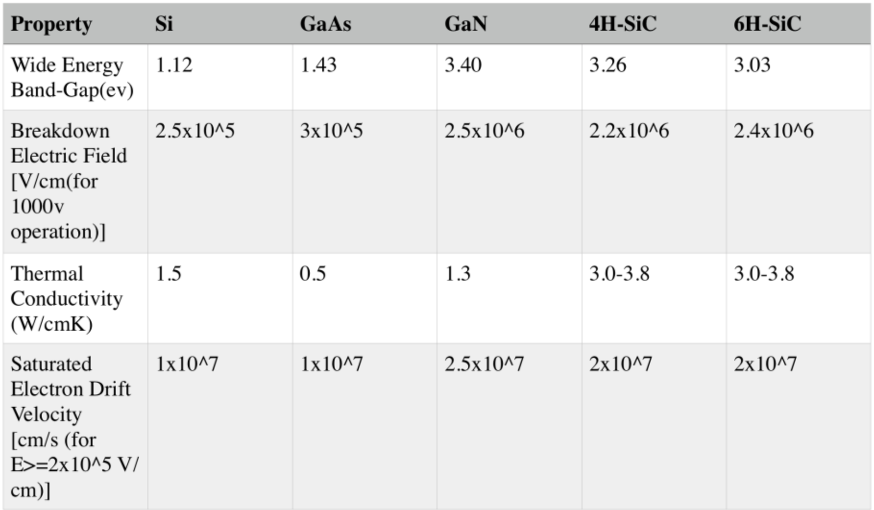

Property	Si	GaAs	GaN	4H-SiC	6H-SiC
Wide Energy Band-Gap(ev)	1.12	1.43	3.40	3.26	3.03
Breakdown Electric Field [V/cm(for 1000v operation)]	2.5x10^5	3x10^5	2.5x10^6	2.2x10^6	2.4x10^6
Thermal Conductivity (W/cmK)	1.5	0.5	1.3	3.0-3.8	3.0-3.8
Saturated Electron Drift Velocity [cm/s (for E>=2x10^5 V/cm)]	1x10^7	1x10^7	2.5x10^7	2x10^7	2x10^7

Table 1-1Physical and electronic properties of SiC compared to other commercial semiconductor materials

As seen in the table above, SiC materials have high saturated electron drift velocity (~2 times higher than Si and GaAs), which allows SiC devices operate at high frequencies (Radio frequency and microwave) [2]. Besides, SiC materials have high thermal conductivity (~2 times higher than Si, GaAs, even GaN), which shows that heat flows more easily through SiC than other semiconductor materials. This property makes SiC devices available to work at relatively high power levels while still dissipate a large amount of excess heat. The wide band-gap of SiC materials (~3 times than Si and GaAs) also contribute to the SiC devices operate at high temperature without intrinsic conduction effects.

The two basic components in power devices are diodes and transistors. After the discovery of first SiC device - SiC Schottky diode, SiC JFET and SiC MOSFETs were developed and gradually became commercially available. It is predicted in a recent literature that the global market share of SiC power devices will be $3 billion per year by 2020. [3] The huge market potential shows that as a promising power device, SiC will continuously play tremendous important role in the near future.

SiC crystals have over 200 types of different polytypes, among which the most common ones are 3C, 4H, 6H and 15R (15R was the first found structure).

- The letter “C” in “3C-SiC” means “cubic” and “3” refers to the minimum number of repeating stacking sequence between layers (ABC).
- The letter “H” stands for “Hexagonal” and hence the stacking sequence for 4H-SiC and 6H-SiC are “ABA’C’...” and “ABCB’A’C’…” separately (B’ means twinned structure of B).
- The letter “R” shows that the structure of 15R-SiC crystal is “Rhombohedral” and the stacking sequence is “B’A’BCAC’B’CABA’C’ABC…” To illustrate it, for 4H-SiC structure, the symmetric stacking of 2 untwined tetrahedral followed by 2 twined, while the 3 untwined tetrahedral followed by 3 twined for 6H-SiC structure as shown in figure 1-1.

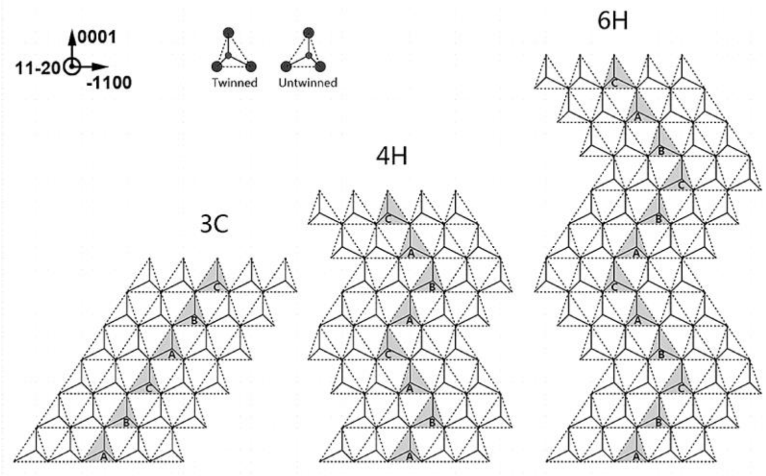

Figure 1-1 Stacking sequence of 3C-, 4H- and 6H-SiC

Those various stacking sequences lead to huge differences in physical and thermal properties between different kinds of SiC. Some of the important properties of 3C-, 4H- and 6H SiC are listed in table 1-2.

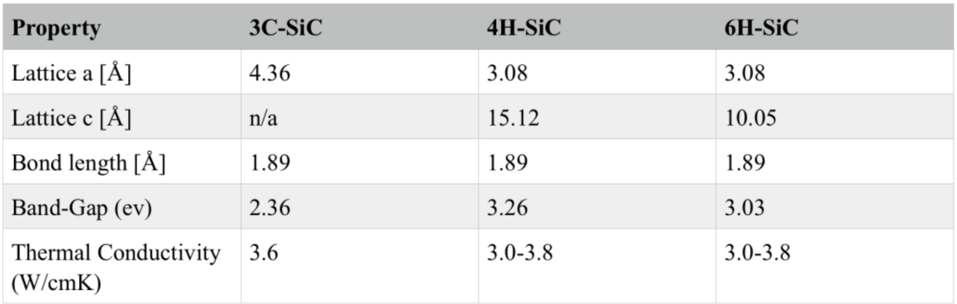

Property	3C-SiC	4H-SiC	6H-SiC
Lattice a [Å]	4.36	3.08	3.08
Lattice c [Å]	n/a	15.12	10.05
Bond length [Å]	1.89	1.89	1.89
Band-Gap (ev)	2.36	3.26	3.03
Thermal Conductivity (W/cmK)	3.6	3.0-3.8	3.0-3.8

Table 1-2 Key parameters of 4H-, 6H- and 3C SiC

1.2 Crystal Growth Technique for SiC

Acheson synthesized the first "artificial crystalline carbonaceous material", which is defined as Carborundum in his early 1892 patent (the term was the combination of "Carbon" and "Corundum", showing the hardness of the material. [4] At that time, the new compound was expressed in the formula of SiC, and was called Silicon of Carbon or carbide of Silicon. However, until 1955, Lely [5] developed a new growth process - generating SiC buck crystal on a porous SiC cylinder using vapor condensation. Followed by Tairov and Tsvetkov in 1978[6], the seeded sublimation growth was gradually becoming a leading method and mature process. In fact, the work of Tairov and Tsvetkov made a milestone in developing Lely Technique, which makes it possible to control the growth of large size SiC wafers on seeds. The modified Lely Technique is often referred as Physical Vapor Transport (PVT) growth and was refined and widely used by numerous companies. In the early 1991, the Cree Research Inc[7]. opened the market entrance for the first commercial 1 inch(25mm) SiC wafer. Nowadays, 3 inch (75mm), 4 inch (100 mm), even 6 inch(150mm) wafer are widely market available using PVT method.

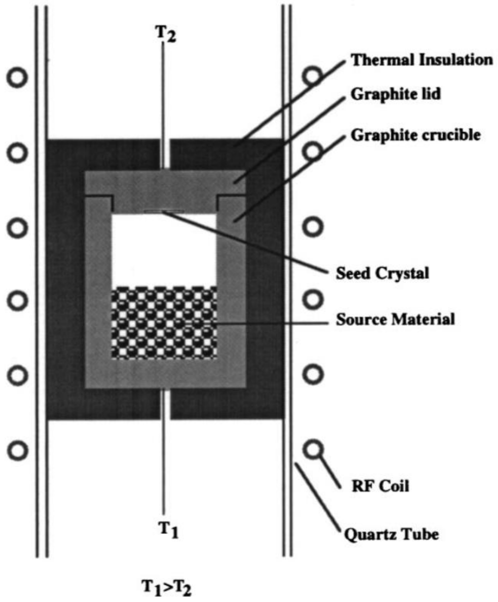

Figure 1-2 Schematic of the PVT method [9]

Figure 1-2 shows the principle of sublimation reactor, which is currently a standard growth technique for bulk SiC single crystals. The main idea is to sublime SiC powder at relatively high temperatures (1800◦ C -2600 ◦ C) and to re-crystallize the Si- and C-containing gas species at a single crystal seed. [8] The seed crystal is mounted on the top of the crucible while the source material (SiC powder) is held at the bottom. RF coils around the crucible are used to heat up the crucible during the whole process. The desirable values for the source could be 2300 ° C and 2100 ° C for the seed. Obviously, temperature is an essential parameter during crystal growth. The growth temperature with Si/C ratio together may affect the polytype of the growing crystal. For example, according to R. Yakimova [9], 4H-SiC crystal growth process is very sensitive with the temperature as it owns an extremely narrow temperature period (2350 ° C - 2375 ° C). Therefore, if the temperature is lower than 2350 ° C, the crystal quality could be low;

however, if the temperature is higher than 2375 ° C, a polytype conversion (from 4H to 6H) would happen. Besides temperature, stress is another significant factor that needed to be considered as it impacts the dislocation density distribution inside crystals. It has been proved that when the resolved shear stress on a primary slip system exceeds a certain value, multiplication dislocations would be produced. That value is so-called *critical resolved shear stress(CRSS)*. [10]

History shows the goal of long tradition of development of hetero-epitaxial layers (film and substrate are different materials) is to meet the need of high material perfection and the large bulk SiC substrate. [11] The latter, obviously, was no longer a question since early 1991. Actually, after the availability of commercial SiC bulk crystals, research had been motivated on the epitaxy growth on the substrate. A well-developed method is refereed as Chemical Vapor Deposition (CVD). This method is firstly applied by Nishino et al. [12] for growing 3C-SiC on Si substrate. Nowadays, homo-epitaxial (film and substrate are the same materials) growth of SiC using the CVD technique is one of the key prerequisites in manufacturing high performance SiC devices.

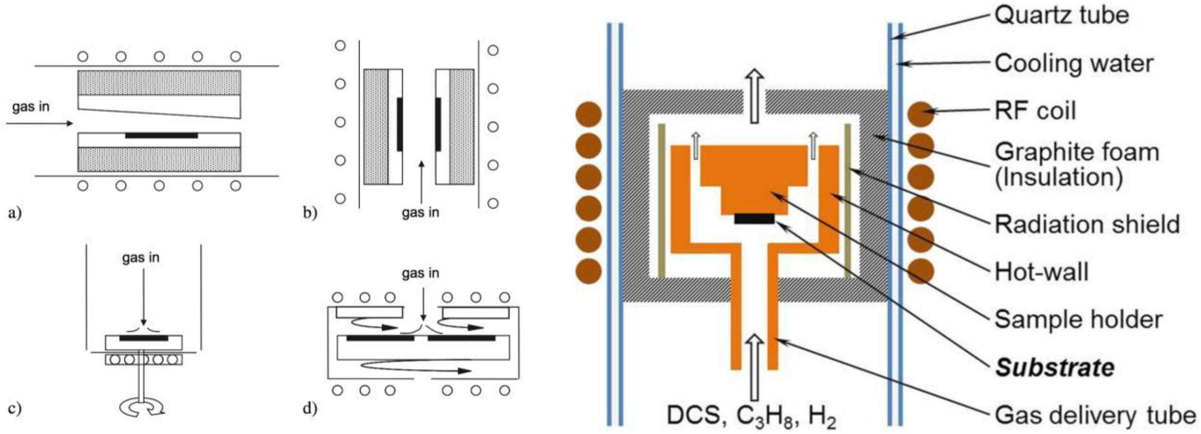

Figure 1-3 Schematic drawings of the most commonly used CVD reactors. [11,13]

Figure 1-3 shows several designs of the CVD reactors that are normally used by companies. For example, in the left figure, (a) shows a horizontal hot-wall reactor while (b) shows a vertical hot-wall reactor. Those two configurations are defined in terms of the direction of reactive gas flow. (c) shows a vertical cold-wall reactor. The difference between hot-wall, cold-wall is determined by their different surrounding designs. (d) shows a multi-wafer rotating planetary reactor in hot-wall configuration.

The right figure of Figure 1-3 shows a hot-wall vertical CVD reactor which uses DCS and C_3H_8 as precursors (DCS for Si, C_3H_8 for C), and H_2 as the carrier gas flow. It has been proved that DCS is a promising precursor to achieve high purity 8° off-axis SiC epilayers at a high growth rate. [14] This also shows that growth of SiC epitaxial layer is more precise controllable with regard to growth rate, doping level, layer thickness, as well as vapor composition. Hence it is more reproducible than bulk PVT method and generally accepted as the most promising technique.

1.3 Defect Structure and Reduction in SiC

Although SiC keeps being a promising candidate for power device fabrication, it cannot be denied that the current state of SiC crystal growth technology delays even the state of Si wafer technology in the 1960s, mainly due to the present of defects repeatedly appear in bulk substrates and epitaxial layers. [15] A comparison between Silicon and SiC wafer technologies as shown in the following figure will better illustrate this scene.

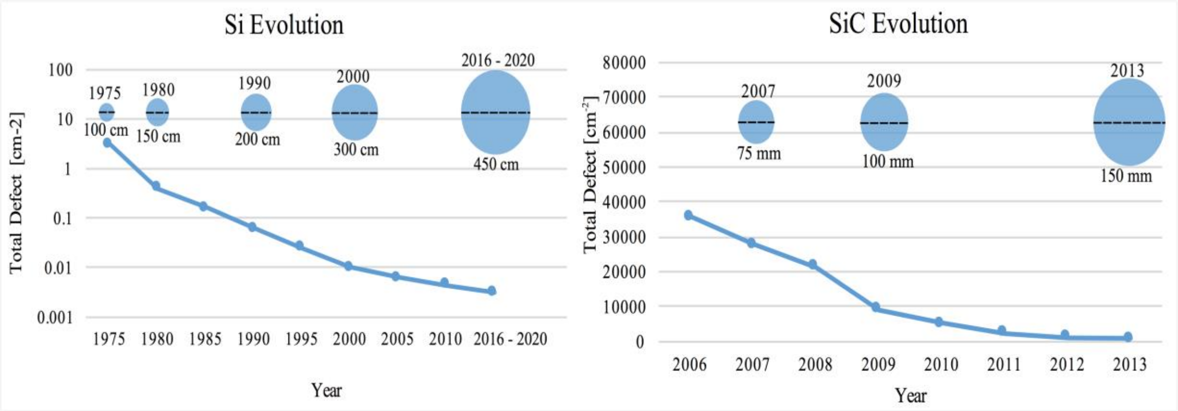

Figure 1-4 Evolution of Si and SiC wafer technologies

The data [16] shows the systematic trend of reducing defect densities for both Si and SiC. Soon after the the first Silicon crystals were grown in 1950, dislocations-free 0.5-inch (12mm) Silicon wafers were produced in 1958. [17] Advancement was made to product defects-free 12-inch (300 mm) wafers in 2001[18]. With this trend, the 18-inch (450mm) defects-free Silicon wafers are expected to be produced in the coming future. However, compared with Silicon wafers, the defect density level of SiC crystals are still so high, around 10^3-10^4 (cm^{-2}). Hence, the understanding of the role that crystal defects play on device performance and long-term reliability is very necessary. Specifically, a better knowledge of the mechanism and properties of defects such as the origin, formation, distribution is needed, subsequently find a way to minimize, even eliminate those defects. For the case of SiC, the common defects are known as 1D defects - dislocations, and 2D defects- stacking faults, grain boundaries. In this thesis, the author mainly focuses on the characteristics of dislocations.

Dislocations can be divided into two categories: growth dislocations and post-growth dislocations (deformation-induced dislocations). It is easy to tell from the definition that growth-in dislocations are formed during growth via replicating dislocations connected with growth interface. For example, if the seed already has dislocations, it could be an origination of continues dislocations. Those growth dislocations are typically straight-lined, and move along well-defined directions depending on the Burgers vector and elastic constants of crystals. [19] Threading dislocations (TDs), including Threading Screw Dislocations (TSDs), Threading Edge Dislocations (TEDs), Threading Mixed Dislocations (TMDs) and Micropipes (MPs) which we will review later, belong to growth dislocations that nucleate at growth front and inherit from the seed.

Deformation-induced dislocations are usually generated behind growth front. Those are formed during the growth process, either by thermal stress or multiplication of pre-existing dislocations. For example, Hopping Frank-Read source mechanism contributes to the Basal Plane Dislocation (BPD) generated in SiC crystal.

As mentioned before, the types of dislocations normally observed in SiC single crystals are TSDs, MPs, TEDs, and BPDs. The nature of dislocations is determined by the Burgers vectors and dislocation line directions. Table 1-2 organize basic characters of those dislocations in SiC single crystals.

Dislocations	Dislocation Line Direction	Burgers Vector(b)
TSDs	[0001]	n[0001],n=1,2
MPs	[0001]	n[0001],n>2(interger)
TEDs	roughly parallel with [0001]	1/3[11-20]
BPDs	(0001)plane	[11-20]

Table 1-3 Configurations of various types of dislocations.

Accordingly, Figure 1-5 shows the Burgers vector and dislocation line directions of BPD, TSD and TED.

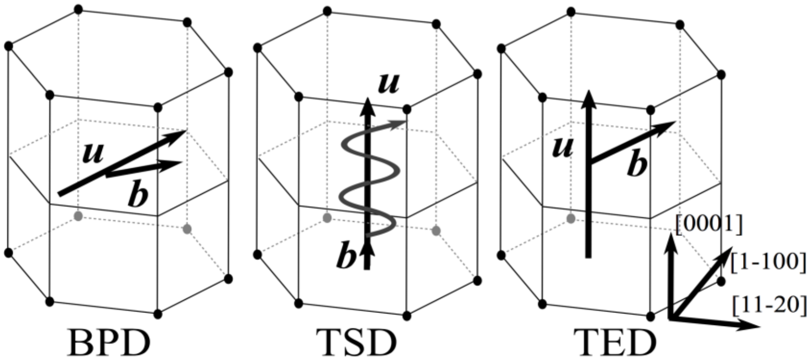

Figure 1-5 (from left to right) A straight BPD in (0001) basal plane; A TSD along [0001] line direction with n [0001] Burgers vector; A TED along [0001] line direction with Burgers vector on basal plane

1.3.1 Micropipe (MP)

The Burgers vector directions of both TSDs and MPs along c-axial, however, MPs own the larger magnitude Burgers vector than TSDs according to Table 1-2. This was proved by Dudley et al. [20], who first topographically observed the MPs (hollow-core screw dislocations) in 1995. Followed by that, in 1999, X.R. Huang et al. [21] used back reflection topography revealed both MPs and TSDs in a 6H-SiC wafer, and successfully simulated the contrast of a MP using ray tracing simulation. The simulated image matched very well with original topographic feature, and strongly reinforced that MPs are pure screw dislocations with giant Burgers vector (between 2c to 15c for the case of 4H-SiC and 6H-SiC [22]). Figure 1-6 shows a MP is seen as a noticeable contrast of white circular spots surrounded by black rings.

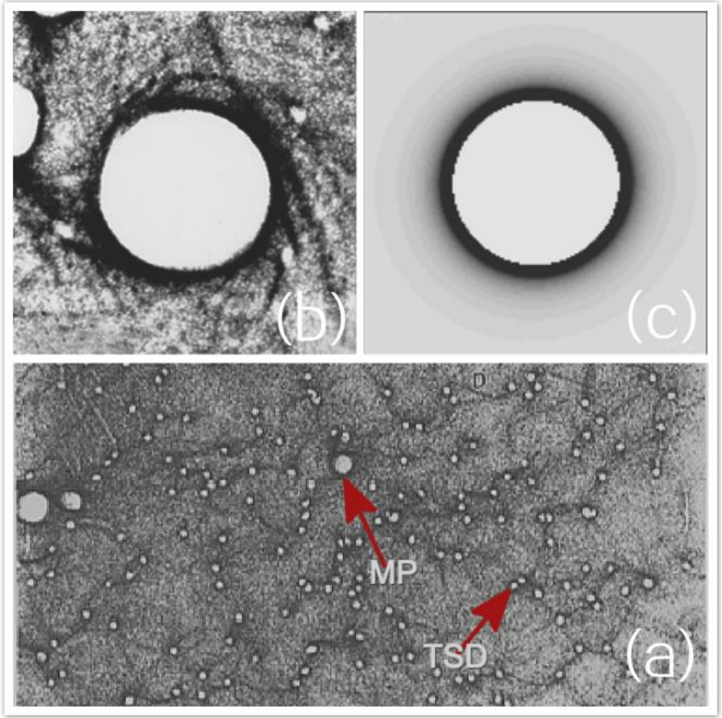

Figure 1-6 (a) Back reflection image for 6H-SiC wafer contained MPs and TSDs; (b) and (c) show an enlarged MP and accordingly simulation result [21]

Since MPs are considered as device-killers in the way of reducing the breakdown voltage while increasing the reverse leakage current level of devices [23], the elimination of MPs in SiC had been a major problem in both research and commercial used since the late 90s. Statics are gathered the overall progress of reduction of MPs from 2009 to 2011 year at Dow Corning (Figure 1-7). The MP densities in both 4inch and 6inch 4H-SiC decreased rapidly in less than 2 years. Nowadays, MP-free SiC are made by some big companies such as Cree Research Inc. and Dow Corning. This a huge breakthrough and hence bring the research into the next stage, concentrating more on the reduction of other types of dislocations.

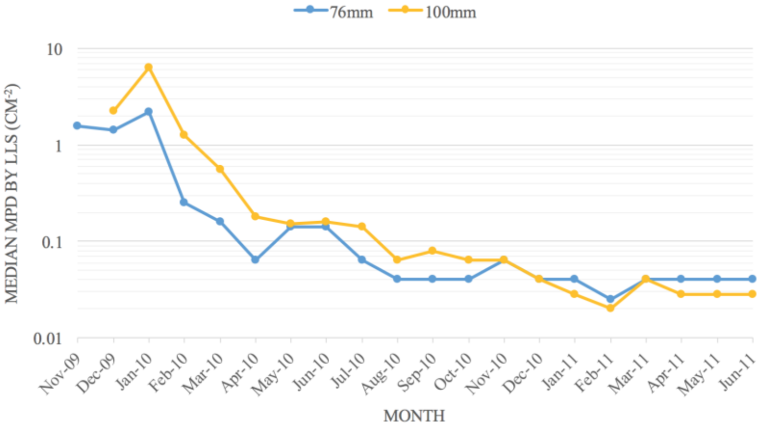

Figure 1-7 Reduction of MP densities in Dow Corning 76 mm and 100 mm 4H-SiC wafers [24]

1.3.2 Threading Screw Dislocation (TSD)

Another type of screw dislocations is threading screw dislocation (TSD), which is also known as closed-core screw dislocations. Compared with MPs, TSDs are less harmful but still cause degradation of device performance via reducing the breakdown voltage by 5-35%. [25] This phenomenon was proved by Neudeck et al in 1999. Figure 1-8 shows a semi-logarithmic plot of TSD density vs breakdown voltage.

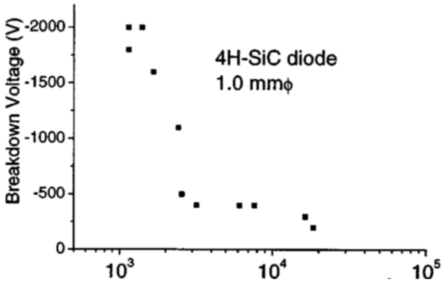

Figure 1-8 TSD density vs breakdown voltage in 4H-SiC diode (2000 year) [26]

The nucleation mechanisms of TSD formation were widely investigated. For example, Dudley et al [27] proposed that TSD can be formed during overgrowth of second phase precipitates on the interface. As TSDs are able to propagate into epitaxial layers along <0001> direction during CVD growth, the density in the epilayers is similar to that in substrate. Recent years, with the optimize growth condition, TSD density decreased dramatically about 1 order of magnitude from thousands (<500 cm $^{-2}$) in both SiC substrates and epilayers. However, the dislocation densities are still high enough to restrict the device achieve full potential. Figure 1-9 shows the reduction of TSD densities in epilayer and substrate separately.

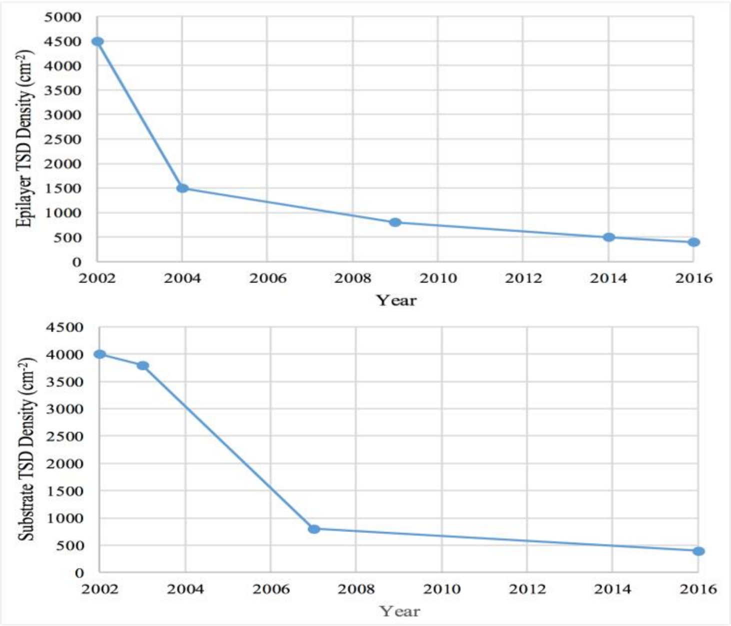

Figure 1-9 TSDs reduction trend in SiC epilayer and substrate from 2002-2016

1.3.3 Threading Edge Dislocation (TED)

Compared with TSD, another type of threading dislocations - threading edge dislocation (TED) seemed not that detrimental to the quality of SiC devices. There are two main sources that contribute to the formation of TED. Takahashi et al [28] proposed that TEDs are grown-in dislocations and most of the TEDs in the substrate are propagated from the SiC seed crystal, then propagated into the epilayer. Besides, conversion of BPD in the substrate into TED has been proposed by Ha et al. [29]. T.Ohno et al. [30] observed the same phenomena in 4H-SiC. BPDs conversion attract a lot of investigations as 70% - 90% of the BPDs in the substrate could become less harmful TED even via conventional epitaxy. [31] With optimizing techniques, for example, by adjusting the C / Si ratio or speeding the growth rate, make 80% - 90% conversion available. [32] In 2005, Chen et al. reported that lower offcut angle (4°) enhancs the conversion of BPD into TED, which makes the BPD density of 4H-SiC epilayer as low as 2.6 cm^{-2}. [33] In 2015, Sudarshan et al. [34] applied a non-destructive pretreatment method on the SiC substrate surface, which allow a grown-on epilayer achieved extraordinary high BPD conversion rate (up to 99.8%) and makes BPD-free 4H-SiC available.

As a big part of BPD convert into TEDs during epitaxy growth, it causes a high TED density in epilayers (10^4 cm^{-2} 12 years ago). It seems that TED received less attention compared with other dislocations (i.e. MPs) due to the less negative effects on performance of SiC devices. Statics shows that the normal density of TED in the substrate is around 10^3 cm^{-2}, without much progress made in dislocations reduction, while line defects in SiC epilayer is reduced by one order of magnitude due to the decease of BPD densities.

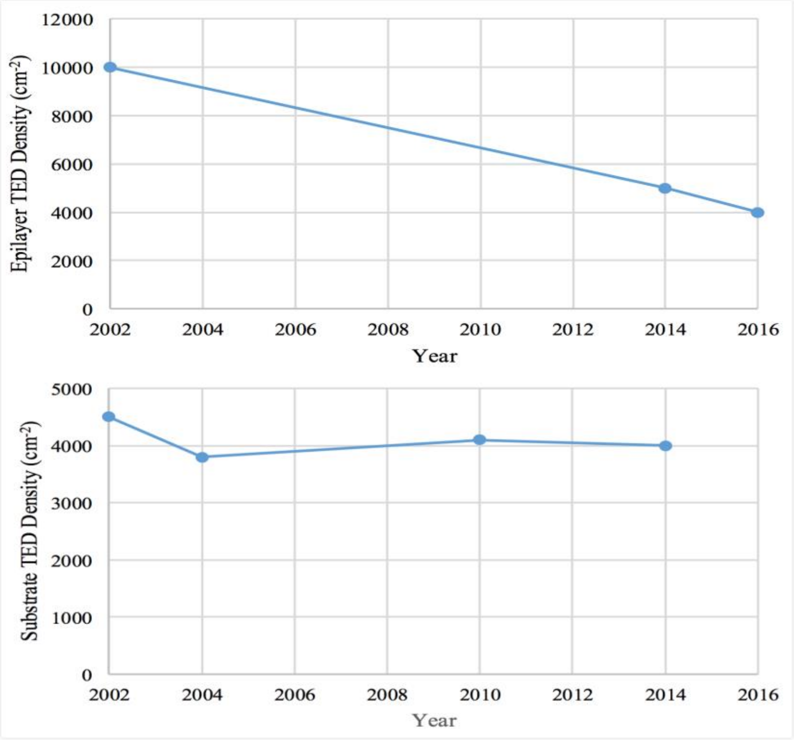

Figure 1-10 TEDs reduction trend in SiC epilayer and substrate from 2002-2016

However, the TEDs have predictable potential causing deleterious effects on device performance. On the one hand, it is not always a good scenario when BPDs convert to TEDs. Recently, Dudley et al. [35] reinforced the fact that certain kinds of conversion may actually contribute to the formation of Interfacial Dislocations (IDs) and Half-loop arrays (HLAs), which are well-known in inducing forward voltage drop and affecting the device performance. This occurs when non-screw type BPDs half-loop segments convert to TEDs. To better illustrate this phenomenon, a short literature review of the mechanism of BPDs conversion will be introduced.

First, for screw type BPDs, it is widely accepted that the segments of BPDs directly interact and then replicate via the interface during the epitaxial growth, generating HLAs and IDs when the critical thickness is reached (Matthews-Blakeslee model) [36]. In contrast, non-screw oriented BPD segments, when intersecting with the interface, are able to convert to TEDs during the epitaxial growth process. This is the main motivation that contributes to the investment of BPD conversion. According to the data that mentioned before, BPDs conversion rates up to 99.8% while the remaining 0.2% are usually screw type dislocations. [13] Nevertheless, one case that needs to be paid attention to is the non-screw oriented BPD half loop in the substrate gradually form IDs and HLAs, which is initially from two intersection points converted to TEDs. This scene will be illustrated in the following figure.

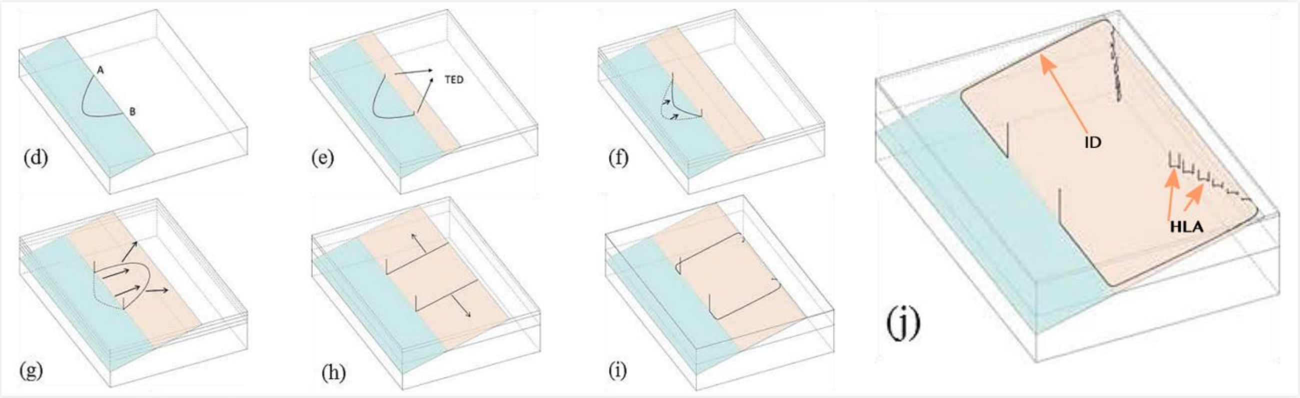

Figure 1-11 (d)- (j) Formation mechanism of pairs of IDs and half-loop arrays. [35]

Figure 1-11 schematically shows the formation mechanism of pairs of IDs and half-loop arrays. A non-screw oriented BPD half loop intersects with the substrate surface at both ends (As A and B shown in the figure above). Since the intersections are not in pure screw directions, they are prone to convert to TEDs during epitaxial growth (Fig. (e)). Then due to the temperature gradient in growth chamber, compressive thermal stress “drag” the pinned half-loop glide towards the substrate interface, as shown in Figure 1-11 (f) and (g). Finally, the half-loop passes through the epilayer and escapes through the advanced epilayer surface, leaving two straight screw BPD segments of opposite sign (Fig.(h)). Those BPD segments will continue replicate and glide under Matthews-Blakeslee model, creating pairs of IDs and HLAs simultaneously (Fig. (j)).

On the other hand, it is worth highlighting that TEDs will eventually degrade the performance of SiC devices as they provide various sources in generating BPDs both in the substrate and epilayers. This will be reviewed in the next part.

1.3.4 Basal Plane Dislocation (BPD)

Basal plane dislocations (BPDs) are dislocations observed on the basal plane (ie. (0001)), which are considered as performance limiting defects in SiC devices. It has been proved that BPDs can produce expanding stacking faults, leading to bipolar power device degradation and reduction in carrier lifetime. [37] These problems, however, can be eliminated by reducing the BPD densities in the epilayers. Investigations have been taken around 20 years, and zero-BPD SiC is successfully generated in 2015. Milestones of the developments of BPD densities reduction both in epilayers and substrates is shown in Figure 1-12.

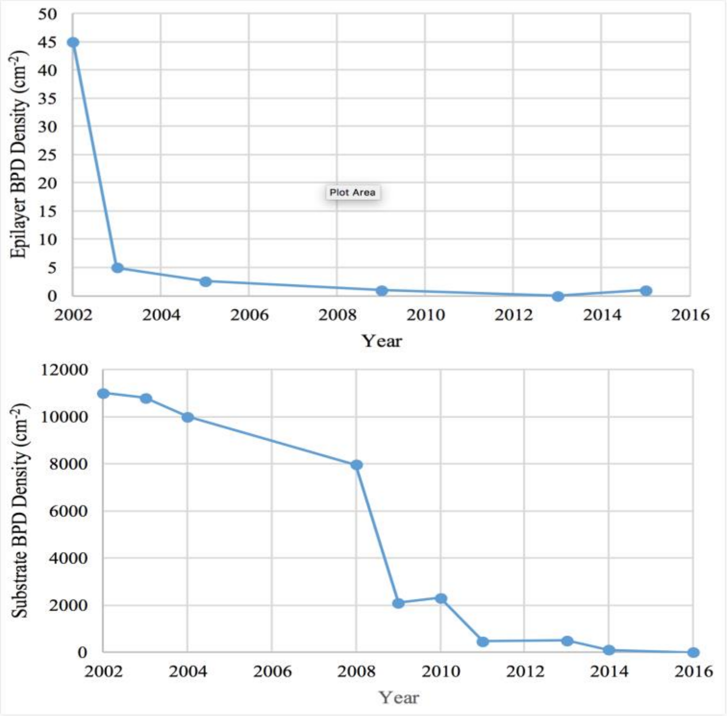

Figure 1-12 BPDs reduction trend in SiC epilayer and substrate from 2002-2016

BPD density reduction in both epilayers and substrate and has been widely researched since the early 2000s. A significant method by converting BPDs in the substrate into TEDs was first proposed by Ha et al. [29] in 2002. With the use of this method, the density of BPDs in the epilayers could be reduced as low as 4-5 cm^{-2}. Later Chen et al. [33] reported that lower offcut angle (4°) enhanced the conversion of BPD into TED, making the BPD density of 4H-SiC epilayer is 2.6 cm^{-2}. In 2015, the optimized technique was applied by Sudarshan et al. [34], and BPD-free SiC was obtained. For BPDs in SiC substrate, a modified PVT growth was developed in 2009, which enabled the growth keeping under the CRSS and hence lower the densities by almost one magnitude. [38]

The BPD densities keep going lower from 2011 to present. Nevertheless, the decreased densities are mainly due to the conversions from substrate BPDs to TEDs, which as mentioned before may cause even worse situations that harm (IDs and HLAs). Therefore, it is necessary to understand the mechanism of BPD nucleation and multiplications during epitaxy growth.

BPDs are deformation-induced dislocations and are readily to nucleate at both crystal edges or other defect sites (i.e. MPs, inclusions). The multiplication of BPDs in the SiC crystal has been widely investigated in the past decades, yet no clear understanding of the mechanism is obtained. A dominant mechanism - Hopping Frank-Read Source Mechanism for BPDs in 4H-SiC was reported by H. Wang et al. [39]. According to this mechanism, the repeated inter-conversion between TEDs and BPDs under shear stress results in glissile BPD segments on parallel basal planes pinned by TED segments. Then, they will undergo multiplication through single - ended Frank-Read source. Figure 1-13 systematically shows the principle of this mechanism and the observations in real topographs.

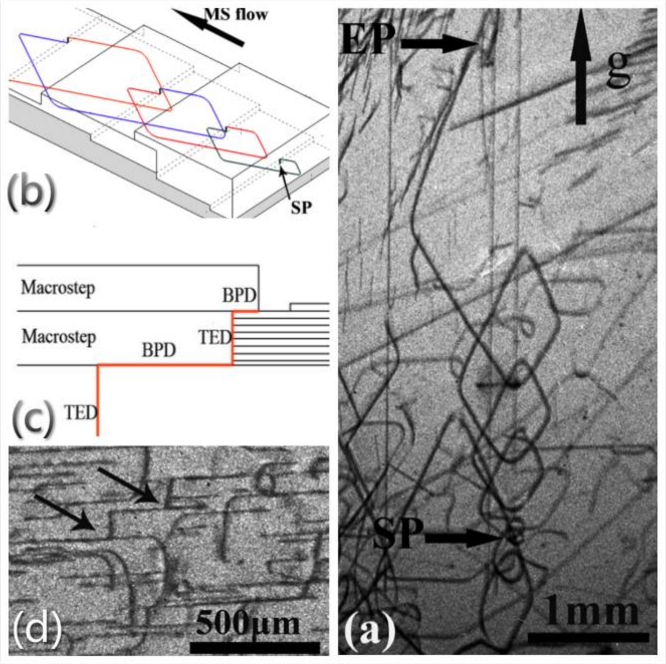

Figure 1-13 (a) Synchrotron X-ray image recorded from a 4H-SiC wafer; (b) The loops produced by the Hopping Frank-Read mechanism; (c) Schematic cross-sectional view of the process; (d) Synchrotron X-ray image confirming the existence of the double deflection process between TED and BPD segment [39]

First, this mechanism can start from either BPDs or TEDs. Figure (c) shows a process begin with a TED. TED is observed glide on the prismatic planes in SiC crystals. The glide of TED will generate screw oriented BPD segments on the basal plane. The overgrowth of macrostep on a TED can also deflects it onto the basal plane and form BPD, followed by the operation of a single-ended Frank-Read source. [40] The starting point (SP) is shown in Figure (a) and (b). Then, if the advancing macrostep encounters an opposite direction step (i.e. a spiral step associated with TED), the BPD segments will convert into TED segments. Lately, as another macrostep advances, TED is re-deflected, leaving a BPD segment on another basal plane. The whole process is expressed in Figure (c) and the observation of the "hopping" existence is presented in synchrotron X-ray image (Fig.(d)). Accordingly, with more macrosteps keep advancing, TED single-ended source is repeatedly formed on different basal planes. Besides, in order to overcome the mutual repulsive forces between loops, they must be sufficiently separated from each other, forming superimposed-shape loops as shown in Figure(a).

2. Characterization Technique

2.1 Synchrotron X-ray Topography (SXRT)

Multiple techniques have been employed to characterize semiconductor single crystals such as Transmission Electron Microscopy (TEM), Scanning Electron Microscopy (SEM), Selective Chemical Etching (melted KOH), etc. Synchrotron X-ray Topography, a widely-used, non-destructive, and powerful characterization technique, is primarily used in our research. Basically, our experiments were done at National Synchrotron Light Source (NSLS) - Beamline X19C, and Advanced Photon Source (APS) - Beamline 1BM, etc. The schematic experimental setting-ups are illustrated in Figure 2-1.

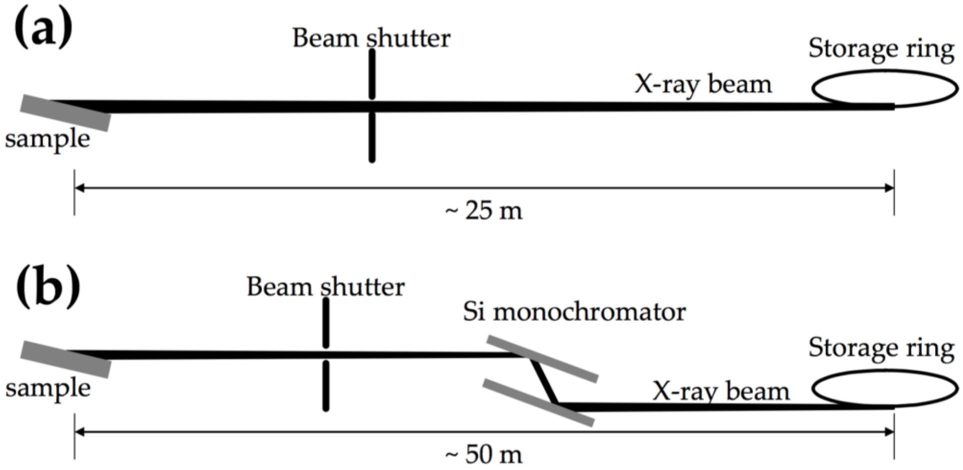

Figure 2-1 (a) Synchrotron White Beam X-ray Topography (SWBXRT); (b) Synchrotron Monochromatic X-ray Topography (SMBXRT)

Compared with traditional source, synchrotron X-ray source has significant advantages [41] as listed below:

- High density. It is round 5-6 orders of magnitude more intense than conventional sealed tube source.
- High efficiency. In conventional source, most of the kinetic energy is converted into heat when high speed electrons collide a mental target, hence less than 1% is transformed into X-rays. In Synchrotron source, however, the electrons are accelerated and allowed to continue circulating in a storage ring. [42]
- Natural collimation in vertical plane and therefore cause low divergence.
- Large X-ray area (up to 10 cm width and 1cm height in APS)
- Wide wavelength range (0.2 Å ~ 4.0Å)
- High resolution.

According to Kinney et al., three parameters of X-ray source highly determine the topographic resolution. That is, X-ray intensity, the energy spectrum and the divergence of incident beam. [43] Obviously, synchrotron X-ray source is an ideal source that leads to high resolution X-ray topography development.

Figure 2-1 (a) shows the setting-up used in Synchrotron White Beam X-ray Topography (SWBXRT). When a white beam passes through the beam shutter and impinges on a single crystal, diffraction from sample can take place either in Back-reflection or transmission method as shown in Figure 2-2 (a) and (b).

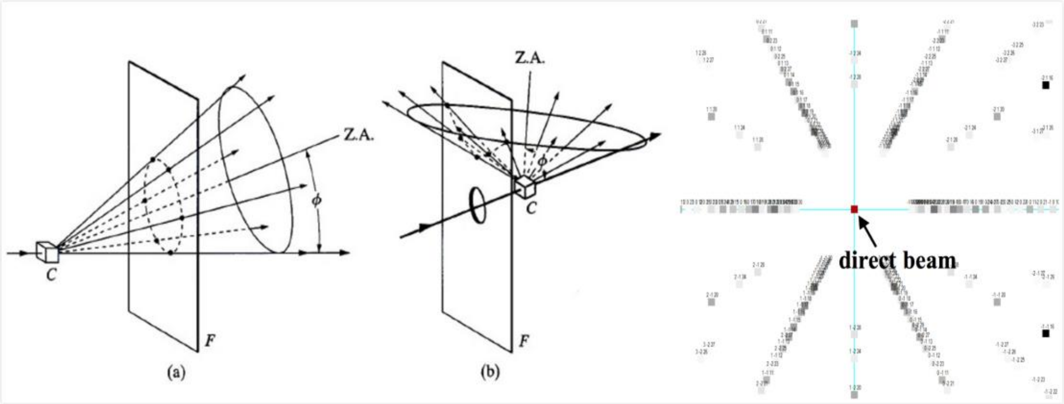

Figure 2-2 Location of Laue spots on (a) Transmission method; (b) Back-reflection method. (C=Crystal, F= Film)

The corresponding diffraction patterns, also called “Laue patterns”, will be created (as shown in the right part in Fig. 2-2) when the beam diffracted in various directions and satisfies the Bragg Law [44]:

$$n\lambda = 2dsin(\theta) \qquad (1)$$

Where λ is the wavelength of incident wave, d is the plane spacing of the diffracted plane, θ is the Bragg angle. For the case of Synchrotron Monochromatic X-ray Topography (SMBXRT), as shown in Figure 2-1(b), only a single diffraction pattern can be obtained. Each spot in a pattern is a high-resolution X-ray topography, which provides a good way for defect analysis as it visualizes the variation of diffracted intensity as a function of position. The density-change is expressed in contrast, and different types of defects give rise to contrast in different mechanisms. Therefore, analysis of variation in contrast will provide much information in corresponding defects characterizations, such as dislocation orientations, Burgers vector etc.

Overall, the priory of SXRT can be summarized as follows:

- High resolution and large sample size allowed.
- Multiple reflections simultaneously (SWBXRT).
  Multiple reflections obtained on one film with different Bragg’s angle set-ups, which lead to an efficient data acquisition. Besides, the multiplicity of images also enables extensive characterization inside crystals.
- Multiple working modes.
  Different geometry set-ups are available, in which different corresponding types of data collected are available. Besides, by controlling the scanning steps in both vertical and horizontal, large size samples (i.e. 6-inch wafers) can be recorded.

The common geometries in our experiments will be introduced in the next part. X-ray topography is recorded by AGFA Structurix D3-SC photographic film. The film-sample distance is set to around 20cm to get the optimize resolution. Then the recorded is developed and fixed in Kodak D19 chemicals providing for future analysis.

2.2 Geometries for Diffraction Images

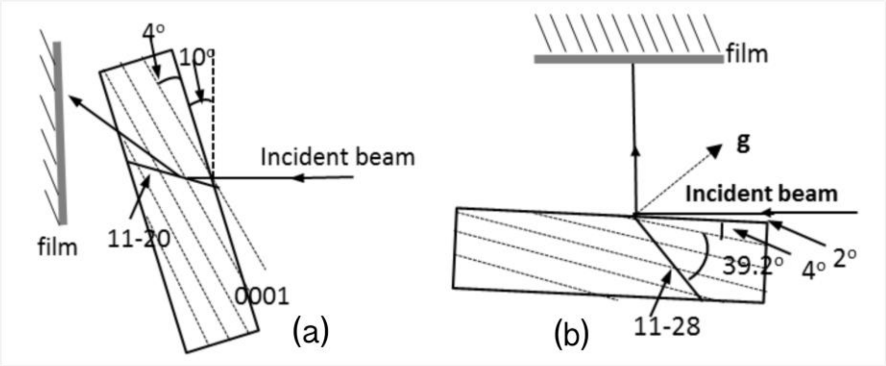

Figure 2-3 (a) Transmission geometry; (b) Grazing geometry

Figure 2-3 (b) and (c) shows transmission geometries (Laue geometries) and grazing geometries separately. As mentioned before, in transmission geometries, the samples are located between the incident beam and film. When the beam passes through the sample, the overall defects information is recorded simultaneously in the film. This method is especially effective for visualizing BPDs inside crystals. Figure 2-4 shows a transmission image for a part of 4H-SiC wafer (Area size:1.5mm x 3mm; Thickness: 368um) with 4˚ off-cut along [11-20] direction. BPD was observed as a dark-curved line with strong contrast. Noted that transmission geometry does not always work for thick samples as they may absorb a large part of radiation and cause the reduction of diffracted beam intensity.

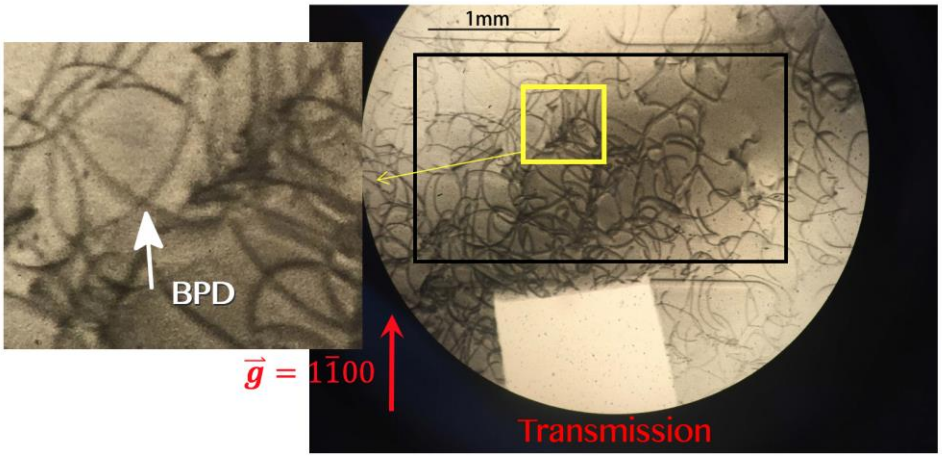

Figure 2-4 Transmission image for a 4H-SiC wafer (area size:1.5mm x 3mm)

Another widely-used geometry in our research is grazing geometry. In this geometry, a very small incident angle is used (normally 2°) and the (11-28) reflection is recorded, as shown in Figure 2-3 (b). The film is mounted on the top of the sample to receive reflections. Noted that the penetration depth of X-ray of grazing geometry is low. This unique characteristic is particularly good for the study of defects near the surface or an epilayer.

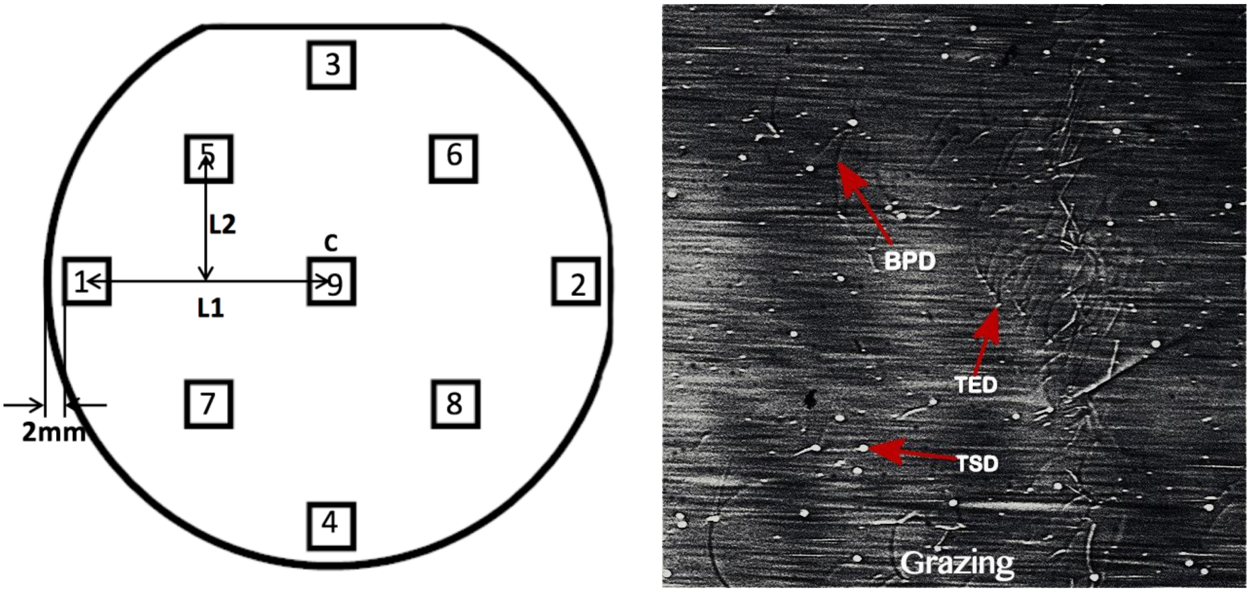

Figure 2-5 Wafer template with selected square regions and the corresponding grazing image in one region

Figure 2-5 shows a grazing image for a 4-inch, 368um 4H-SiC wafer. The right part in the figure is a square region of size 2mm×2mm from the wafer. The left part in the picture above indicates where the square region may be picked from. In fact, with this template, the defect densities shown in the grazing image could be calculated. For example, TSDs and TEDs could be observed in above image with different size configurations. Larger dark spots with roughly oral shape correspond to TSDs, while smaller spots are referred to TEDs with faint contrast. The number of TSDs that show up in this topograph can be counted. Then, the TSD density in this certain region would be the value of dividing the area of selected region by the count.

3. Dislocation Line Direction Analysis and Simulation in 4H-SiC

Due to the presence of dislocations in bulk substrates and epitaxial layers, the performance of SiC devices is limited. It is necessary to minimize and eventually eliminate those dislocations. Dislocation line direction analysis provides an idea tool that can be used to deduce the origins of those dislocations. For deformation-induced dislocations (i.e. basal plane dislocations) that are produced by plastic deformation under thermal stress, the origins of dislocation provide information about their movement in the various slip systems, such as basal plane slip, prismatic slip and pyramidal slip. For grown-in dislocations (i.e. threading dislocations) during the crystal growth process, detailed information about dislocation line directions proved the formation mechanism and trends during growth. For example, recent study [45] shows that a large amount of threading dislocations is mixed dislocations with Burgers vector $nc + ma$ (m and n are integers). These are either inherited from the seed crystals or nucleated at the interface first, then replicated the growth interface during crystal growth. Therefore, the information on dislocation line directions can provide a tendency of dislocation glide and multiplication.

Synchrotron White Beam X-ray Topography allows instantaneous dislocation Burgers vector analysis and line directions analysis by combining several Laue spots recorded in a film. A method, which could trace back the 3D directions of the dislocations inside crystal from two different dislocation images, is reported. This method is a developed based on the research of Yuan Ding and Michael Dudley [45] in 1992.

3.1 Outline

An approach of this method is shown in Figure 3-1. The basic idea is combining the crystal structure, rotation parameters and any two line-directions recorded in the film to trace back the dislocation line directions in real crystal. This method should work for any crystal structure. In this report, hexagonal structure of 4H-SiC has been used to develop a computer program using JavaScript. This program allows for quick data acquisition and better visualization of the 3D positions of dislocation line inside 4H-SiC crystals.

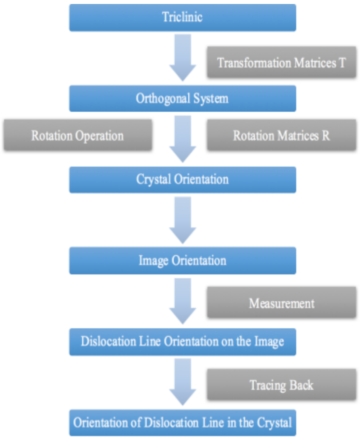

Figure 3-1 Flowchart of program for a given crystal structure

3.2 Calculation Procedure

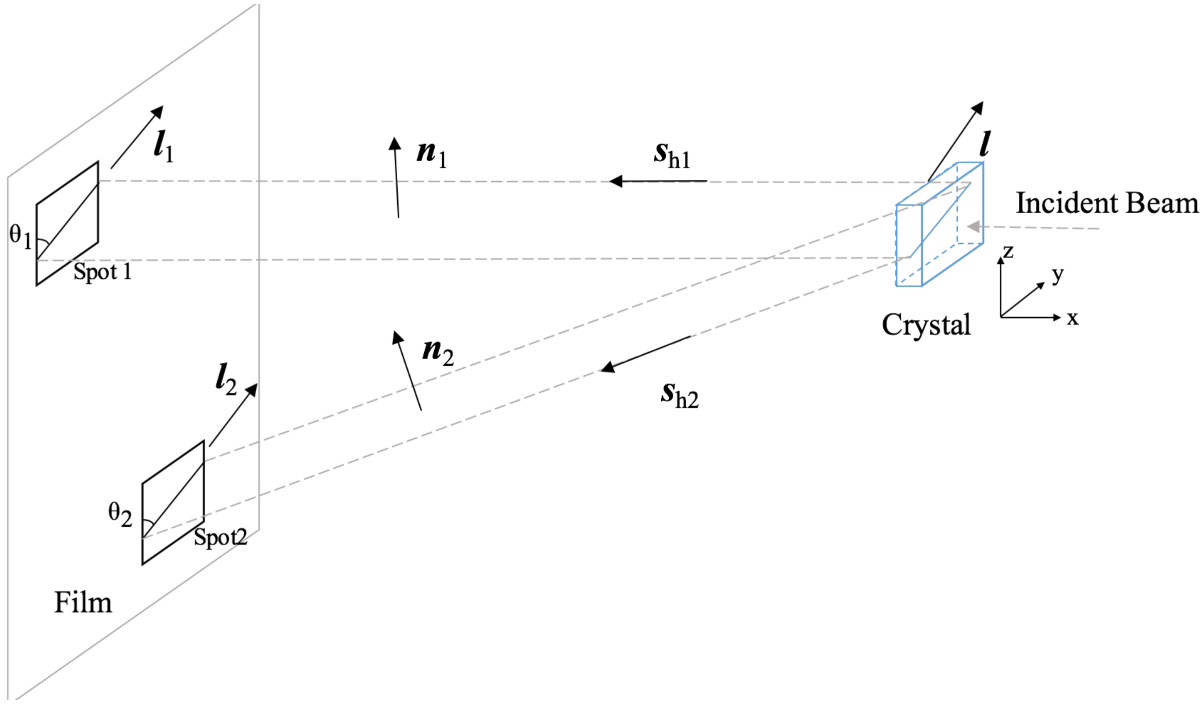

Figure 3-2 Schematic illustrate the principle of finding the real dislocation line direction in the crystal

Figure 3-2 shows the principle of calculation procedure. The sample is mounted in transmission geometry as shown above. When the X-ray beam impinges on the sample, the corresponding diffraction spots (i.e. spot 1 and spot 2) are recorded in the film. Due to the diffraction nature, a dislocation line (l) in the crystal is recorded in both spot 1 and spot 2 with different slope with z-axis. The slit edge (z-axis) is chosen as reference line. The angles between the dislocation lines (l_1, l_2) and the reference line are expressed as θ_1 and θ_2, from which he dislocation line directions (**$\mathbf{l_1}$, $\mathbf{l_2}$**) on the image can be calculated.

Then, the positions of spots are identified by the diffracting vector $\mathbf{S_h}$, The diffraction plane normal $\mathbf{n_1}$ can be expressed by the cross product of $\mathbf{l_1}$ and $\mathbf{S_h}$, while $\mathbf{n_2}$ can be obtained by the cross product of $\mathbf{l_2}$ and the diffracting vector $\mathbf{S_{h2}}$. As shown in the Equation (2) below:

$$\mathbf{n_1} = \mathbf{S_{h_1}} \times \mathbf{l_1}, \mathbf{n_2} = \mathbf{S_{h_2}} \times \mathbf{l_2} \qquad (2)$$

Finally, the dislocation line direction **l** in the real crystal can be determined by the cross product of $\mathbf{n_1}$ and $\mathbf{n_2}$.

$$\mathbf{l} = \mathbf{n_1} \times \mathbf{n_2} \qquad (3)$$

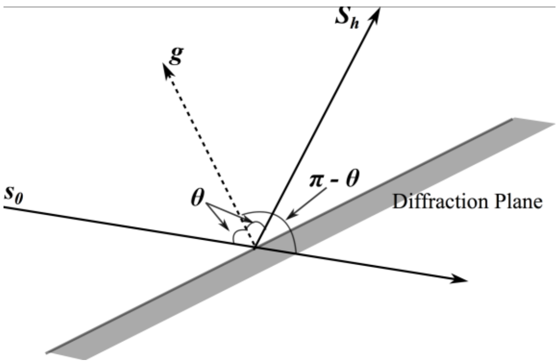

Figure 3-3 Diffraction vector determination

Figure 3-3 shows the way to calculate the diffracting vector **S_h.** Diffraction take place when Bragg's law is satisfied. In this calculation we only consider the diffraction images that are explained by Kinematical theory.

To get the diffraction vector **Sh_1** and **Sh_2**, the incident vector **S_0** and diffraction plane normal **g** are needed. The relation of these three parameters is shown in Equation (4)(5).

$$\begin{cases} \vec{\mathbf{S_h}} \cdot \vec{\mathbf{g}} = -\vec{\mathbf{S_0}} \cdot \vec{\mathbf{g}} & (4) \\ \vec{\mathbf{S_h}} \times \vec{\mathbf{g}} = \vec{\mathbf{S_0}} \times \vec{\mathbf{g}} & (5) \end{cases}$$

An example is given here. Suppose the incident beam along (100), and the diffraction plane is (111). We have **S_0**= (100), and **g**= (111), the **S_h** can be calculated as follows:

According to (3), 1 = - (x + y + z).

According to left hand side of (4):

$$\begin{vmatrix} i & j & k \\ 1 & 0 & 0 \\ 1 & 1 & 1 \end{vmatrix} = 0 - i - k = (0, -1, 1)$$

According to right hand side of (4):

$$\begin{vmatrix} i & j & k \\ x & y & z \\ 1 & 1 & 1 \end{vmatrix} = (y-z)i + (z-x)j + (x-y)k = (y-z, z-x, x-y)$$

Therefore, we have,

$$\begin{aligned} & y = z, x = 1 + z \\ & \Rightarrow z + 1 + z + z = -1 \\ & \Rightarrow z = -\tfrac{2}{3} \\ & \Rightarrow \vec{S_h} = (\tfrac{1}{3}, -\tfrac{2}{3}, -\tfrac{2}{3}) \end{aligned}$$

As the the values of plane normal **g** and incident vector **S_0** vary due to crystal structures and diffraction conditions, these two parameters need to be defined accordingly and will be fully illustrated in the following section.

(1) Plane normal **g**

As mentioned before, X-ray diffraction is the reflection by sets of parallel planes inside crystals. For this situation, we have to consider the orientation and spacing of these sets of planes. There is a conceptual advantage if we think in terms of their normal instead of the planes themselves. For example, we can project these normals onto various surfaces, such as reference planes, stereographic projection, etc. Stereographic projections only give us the relative orientation information; we still need information about the spacing between planes. The concept of reciprocal lattice is preferred as it can visualize both the orientations and inter-planar spacings of the planes of a crystal lattice.

In reciprocal lattice, each parallel set of planes with a given d spacing, is represented by a single reciprocal lattice point. The direction is the plane normal, and the length is the inverse of the d spacing of the set of planes. The reciprocal lattice is constructed using vectors **a*, b*, c***. A general way to define reciprocal lattice is introduced using matrix tense G. [45]

Set

$$G = \begin{pmatrix} \mathbf{a} \\ \mathbf{b} \\ \mathbf{c} \end{pmatrix} \begin{pmatrix} \mathbf{a} & \mathbf{b} & \mathbf{c} \end{pmatrix} = \begin{pmatrix} \mathbf{a}\cdot\mathbf{a} & \mathbf{a}\cdot\mathbf{b} & \mathbf{a}\cdot\mathbf{c} \\ \mathbf{b}\cdot\mathbf{a} & \mathbf{b}\cdot\mathbf{b} & \mathbf{b}\cdot\mathbf{c} \\ \mathbf{c}\cdot\mathbf{a} & \mathbf{c}\cdot\mathbf{b} & \mathbf{c}\cdot\mathbf{c} \end{pmatrix} \qquad (6)$$

Define

$$\begin{pmatrix} \mathbf{a}^* \\ \mathbf{b}^* \\ \mathbf{c}^* \end{pmatrix} = G^{-1} \begin{pmatrix} \mathbf{a} \\ \mathbf{b} \\ \mathbf{c} \end{pmatrix} \qquad (7)$$

to relate the reciprocal lattice vectors with real lattice vectors.

Through organization,

$$G^{-1} = m \begin{bmatrix} \frac{sin^2\alpha}{a^2} & \frac{cos\alpha cos\beta - cos\gamma}{ab} & \frac{cos\alpha cos\gamma - cos\beta}{ac} \\ \frac{cos\alpha cos\beta - cos\gamma}{ab} & \frac{sin^2\beta}{\beta^2} & \frac{cos\beta cos\gamma - cos\alpha}{bc} \\ \frac{cos\alpha cos\gamma - cos\beta}{ac} & \frac{cos\beta cos\gamma - cos\alpha}{bc} & \frac{sin^2\gamma}{c^2} \end{bmatrix} (8)$$

, where

$$m = (1 - cos^2\alpha - cos^2\beta - cos^2\gamma + 2cos\alpha cos\beta cos\gamma)^{-1} \quad (9)$$

For triclinic system,

$$\begin{pmatrix} g_x \\ g_y \\ g_z \end{pmatrix} = \overrightarrow{n} = G^{-1} \begin{pmatrix} h \\ k \\ l \end{pmatrix} \qquad (10)$$

Hence, for a given plane (h k l), the normal of that plane can be calculated through the combination of Equation (8) (9) (10).

Since plane normal information is very primary and essential for the future dislocation line direction analysis, several trials were made to test the validity of these equations. Two examples are described below.

Usually, the unit cell parameters are expressed in terms of angles between the unit cell edges (a, b, c). The vector relations are normally mapped on a Cartesian system. Figure 3-4 shows a diagram in which a rhombohedral unit cell vectors are mapped to a Cartesian system. The dark region shows the plane of (111).

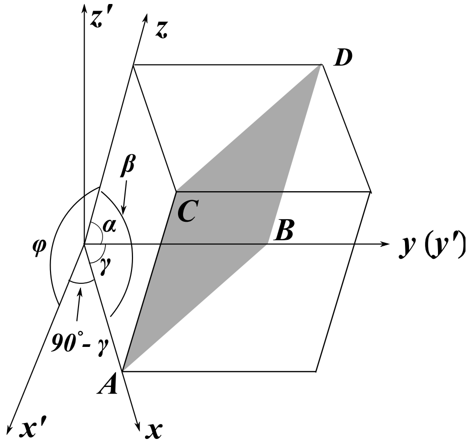

Figure 3-4 Rhombohedral system showing (111) plane mapped to a Cartesian system

The vector relations in a general unit cell is expressed as

$$\begin{cases} \vec{a} = & a \cdot sin\gamma\vec{i} + cos\gamma\vec{j} + 0\vec{k} \\ \vec{b} = & 0\vec{i} + b\vec{j} + 0\vec{k} \\ \vec{c} = & c \cdot sin\varphi\vec{i} + cos\alpha\vec{j} + cos\rho\vec{k} \end{cases} \qquad (11)$$

, in which

$$cos\varphi = \frac{cos\beta - cos\gamma cos\alpha}{sin\gamma} \qquad (12)$$

$$cos\rho = \sqrt{1 - cos^2\varphi - cos^2\alpha} \qquad (13)$$

Define a vector A = (p, q, w) in original rhombohedral coordinate. It can be expressed in triclinic system as

$$\begin{aligned}\vec{A} &= p\vec{a}+q\vec{b}+w\vec{c}\\ &= p\cdot a\cdot sin\gamma\vec{i}+p\cdot a\cdot cos\gamma\vec{j}+q\cdot b\vec{j}+w\cdot c\cdot cos\varphi\vec{i}\\ &\quad +w\cdot c\cdot cos\alpha\vec{j}+w\cdot c\cdot cos\rho\vec{k}\\ &= (p\cdot a\cdot sin\gamma+w\cdot c\cdot cos\varphi)\vec{i}+(p\cdot a\cdot cos\gamma+q\cdot b\\ &\quad +w\cdot c\cdot cos\alpha)\vec{j}+w\cdot c\cdot cos\rho\vec{k} \qquad (14)\end{aligned}$$

For rhombohedral,

$$\because \quad a=b=c$$

$$\therefore \quad \vec{A}=(p\cdot sin\gamma+w\cdot cos\varphi)\vec{i}+(p\cdot cos\gamma+q+w\cdot cos\alpha)\vec{j}+w\cdot cos\rho\vec{k} \qquad (15)$$

Then, we introduce the crystal structure with consideration. Take α-sapphire as example. The crystal information is:

a=b=c=5.13 Å, α=β=γ=55.1°

Set

$$A(1,0,0), B(0,1,0), C(1,0,1), D(0,1,1)$$

$$\overrightarrow{AB}=(-1,1,0), \overrightarrow{AC}=(0,0,1)$$

then,

$$\Rightarrow \overrightarrow{AB}=(-sinr)\overrightarrow{i}+(-cosr+1)\overrightarrow{j}+0\overrightarrow{k}$$

Since $r=55.1^\circ$,

$$\begin{aligned}\overrightarrow{AB} &= -sin55.1^\circ\vec{i}+(-cos55.1^\circ+1)\vec{j}+0\vec{k}\\ &= (-0.82,0.43,0)\end{aligned}$$

Similarly,

$$\overrightarrow{AC}=cos\varphi\overrightarrow{i}+cos\alpha\overrightarrow{j}+cos\rho\overrightarrow{k},$$

$$cos\varphi=\frac{cos\beta-cos^2\alpha}{sinr}=\frac{cos55.1^\circ-cos^255.1^\circ}{sin55.1^\circ}=0$$

$$cos\rho=\sqrt{1-cos^2\varphi-cos^2\alpha}=\sqrt{1-0.3^2-cos^255.1^\circ}=0.76$$

We have

$$\overrightarrow{AC}=(0.3,0.58,0.76)$$

Finally,

$$\begin{aligned}\overrightarrow{AB}\times\overrightarrow{AC} &= \vec{g}=\begin{vmatrix} i & j & k \\ -0.82 & 0.43 & 0 \\ 0.3 & 0.58 & 0.76\end{vmatrix} \\ &= (0.43\times 0.76)\vec{i}+(0.82\times 0.76)\vec{j} \\ &\quad +(-0.58\times 0.82-0.3\times 0.43)\vec{k} \\ &= 0.3268\vec{i}+0.6232\vec{j}-0.6046\vec{k} \quad .\end{aligned}$$

Through Equation (8) (9) (10),

$$\vec{g}=(0.55,0.55,-0.62)$$

If these equations work for rhombohedral system,

$$\begin{aligned}\overrightarrow{g} &= (0.55sin55.1^\circ-0.2cos55.1^\circ)\overrightarrow{i}+(0.55cos55.1^\circ+0.55-0.62cos55.1^\circ)j^\circ \\ &\quad +(-0.62\times 0.26)\overrightarrow{k} \\ &= 0.26\overrightarrow{i}+0.50\overrightarrow{j}-0.47\overrightarrow{k}\end{aligned}$$

, which is consistent with the first result. This proves the equations work for original rhombohedral coordinate (not for Cartesian system).

A second example was applied to an orthorhombic system, taking Heyrovskyie as an example. The crystal information is given by

a=4.14 Å, b=13.72 Å, c=31.5 Å, α=β=γ=90°

Figure 3-5 shows the structure of Heyrovskyie. Similar to α-sapphire, (111) plane inside crystal is shown as shaded region. The Cartesian coordinate is applied along unit cell edges (a, b, c).

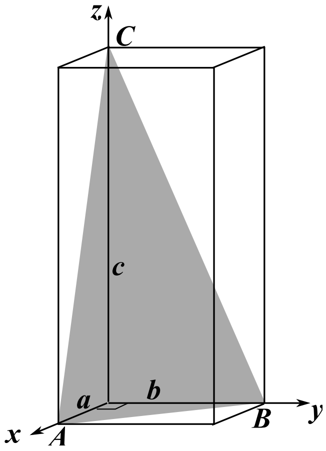

Figure 3-5 Orthorhombic system showing (111) plane

Hence,

$$A(4.14, 0, 0), B(0, 13.72, 0), C(0, 0, 31.5)$$

and

$$\overrightarrow{AB} = (-4.14, 13.72, 0), \overrightarrow{AC} = (-4.14, 0, 31.15).$$

The normal is by the cross product of AB and AC.

$$\begin{array}{lcl}
\overrightarrow{AB} \times \overrightarrow{AC} & = & \begin{vmatrix} i & j & k \\ -4.14 & 13.72 & 0 \\ -4.14 & 0 & 31.5 \end{vmatrix} \\
 & = & (13.72 \times 31.5)\overrightarrow{i} + (0 + 4.14 \times 31.5)\overrightarrow{j} + (0 + 4.14 \times 13.72)\overrightarrow{k} \\
 & = & 432.18\overrightarrow{i} + 130.41\overrightarrow{j} + 56.8\overrightarrow{k} \\
 & \xrightarrow{normalization} & \dfrac{432.18\overrightarrow{i} + 130.41\overrightarrow{j} + 56.8\overrightarrow{k}}{\sqrt{432.18^2 + 130.41^2 + 56.8^2}} \\
 & = & (0.95, 0.28, 0.12)
\end{array}$$

Since $a \neq b \neq c$,

$$\begin{array}{lcl}
\overrightarrow{g} & = & (\dfrac{0.95}{a}, \dfrac{0.28}{b}, \dfrac{0.12}{c}) \\
 & = & (0.23, 0.02, 0.004) \\
 & \xrightarrow{normalization} & (1, 0.086, 0.017)
\end{array}$$

, which again consistent with the result from Equation (8) (9) (10).

Similar analysis was also applied to the Hexagonal system. All these trials show that Equation (8) (9) (10) are applicable only in original coordinate inside crystals. For example, for 4H-SiC, the crystal structure is hexagonal, the original indices based on four axis a_1, a_2, a_3 (120° in between) and c (z-axis). The Miller index is (h k i l) and i=-(h+k). However, the common indices that used in experiments is Cartesian Coordinate with x-axis along [11-20] direction, y-axis along [-1100], z-axisl along [0001] as shown below.

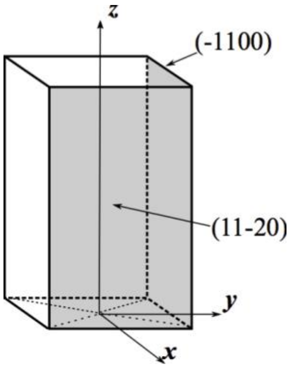

Figure 3-6 Cartesian Coordinate system used during experiments

Therefore, it is necessary to transform and rotate the matrix to coincide the actual use. Figure 3-6 shows the principle of this method (plan view).

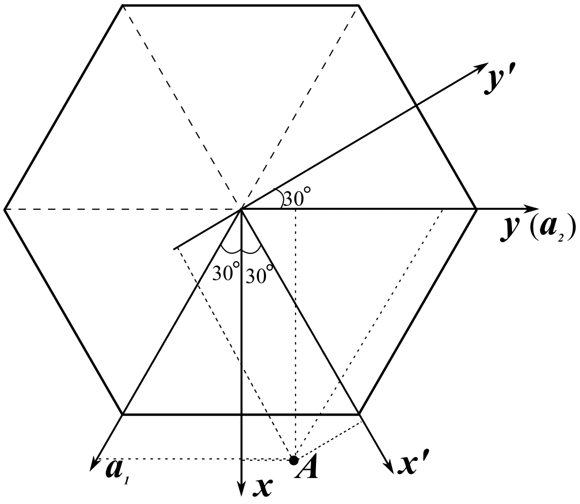

Figure 3-7 Matrix transformation and rotation

Suppose the surface plane of this sample is (10-10). The angle between $a_1$and a_2 is 120°, hence the vectors along $a_1$and a_2 stand for the original coordinates. The x-y coordinate shows the transformed coordinates. Finally, the x-axis along [11-20] direction, y-axis along [-1100] shows it is the coordinate that we want.

Choose any point A= (a_1, a_2, 0) in the original coordinate, we have

$$\begin{cases} x &= \frac{\sqrt{3}a_1}{2} \\ y &= a_2 - \frac{a_1}{2} \end{cases},$$

in an orthorhombic coordinate,

then in the expression of rotation coordinates,

$$\begin{cases} x' &= \frac{1}{2}(a_1 - a_2) + 2(a_2 - \frac{1}{2}a_1) + (a_1 - a_2) = \frac{1}{2}(a_1 + a_2) \\ y' &= \frac{1}{2}(\frac{\sqrt{3}}{2}a_1 - \sqrt{3}(a_2 - \frac{a_1}{2})) = \frac{\sqrt{3}}{2}(a_1 - a_2) \end{cases} \quad (16)$$

Hence, for any $\vec{A} = (a_1, a_2, 0)$ in 120° 3-axials coordinate, we have

$$\vec{A}' = (\frac{1}{2}(a_1 + a_2), \frac{\sqrt{3}}{2}(a_1 - a_2), 0) \quad (17)$$

in the rotated-orthorhombic system.

Now, consider a plane (h k l) in hexagonal system.

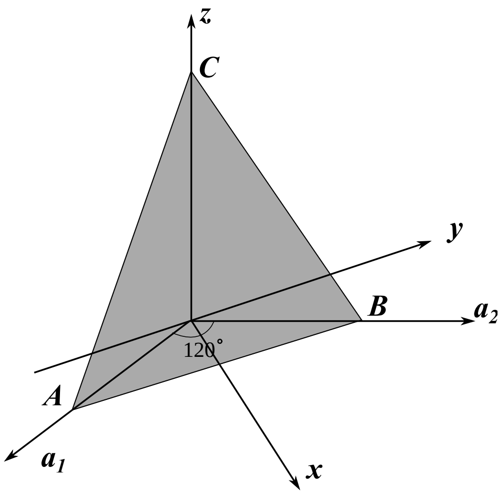

Figure 3-8 A sketch showing a plane in the hexagonal coordinate system

$$A(\tfrac{1}{h},0,0),B(0,\tfrac{1}{k},0),C(0,0,\tfrac{1}{l})$$

$$\Rightarrow \quad A'(\tfrac{1}{2h},-\tfrac{\sqrt{3}}{2},0),B'(\tfrac{1}{k},\tfrac{\sqrt{3}}{2k},0),C'(0,0,\tfrac{1}{l}) \text{ from Equation (17)}$$

According to linear equation:

$$\frac{y-y_1}{y_2-y_1}=\frac{x-x_1}{x_2-x_1}$$

$$\Rightarrow \quad \frac{y+\frac{\sqrt{3}}{2h}}{\frac{\sqrt{3}}{2k}+\frac{\sqrt{3}}{2h}}=\frac{x-\frac{1}{2h}}{\frac{1}{2k}-\frac{1}{2h}}$$

$$\Rightarrow \quad \frac{y+\frac{\sqrt{3}}{2h}}{\frac{\sqrt{3}(h+k)}{2kh}}=\frac{x-\frac{1}{2h}}{\frac{h-k}{2kh}}$$

$$\Rightarrow \quad (y+\frac{\sqrt{3}}{2h})\frac{h-k}{2kh}=(x-\frac{1}{2h})\frac{\sqrt{3}(h+k)}{2kh}$$

$$\Rightarrow \quad (y+\frac{\sqrt{3}}{2h})(h-k)=(x-\frac{1}{2h})\sqrt{3}(h+k) \tag{18}$$

When x=0, the above equation is

$$(y+\frac{\sqrt{3}}{2h})(h-k)=(x-\frac{1}{2h})\sqrt{3}(h+k)$$

$$\Rightarrow \quad y=\frac{-\frac{1}{2h}\sqrt{3}(h+k)}{h-k}-\frac{\sqrt{3}}{2h}$$

$$\Rightarrow \quad y=\frac{\sqrt{3}}{h-k} \quad .$$

When y = 0,

$$
\begin{aligned}
& (y+\tfrac{\sqrt{3}}{2h})(h-k) = (x-\tfrac{1}{2h})\sqrt{3}(h+k) \\
\Rightarrow \quad & x = \tfrac{h-k}{2h(h+k)} + \tfrac{h+k}{2h(h+k)} \\
\Rightarrow \quad & x = \tfrac{1}{h+k}
\end{aligned}
.
$$

New intercepts are

$$\left(\tfrac{1}{H}\,\tfrac{1}{K}\,\tfrac{1}{L}\right) = \left(\tfrac{1}{h+k}\,\tfrac{\sqrt{3}}{k-h}\,\tfrac{1}{l}\right) \qquad (19)$$

Finally, the plane index in rotated-orthogonal system (H, K, L) equals to

$$(h+k)\left(\tfrac{k-h}{\sqrt{3}}\right)(l) \qquad (20)$$

To illustrate it, for (11-20) plane, it can be expressed as (110) in its original coordinate. Then, through Equation (20), it equals to (200) plane in the rotated-orthogonal system.

(2) Incident vector $\mathbf{S_0}$

Until now, for any planes in hexagonal systems expressed in (*hkil*), we can transfer to the coordinate we want expressed in (HKL), then using several equations to calculate the plane normal **g**. Another important factor, incident vector $\mathbf{S_0}$, is determined by the rotation of samples. Sometimes we need to rotate the samples to get the certain diffraction pattern we want during the experiments. This is due to the fact that the angles between incident beam and diffraction plane normal needed to satisfy the Bragg's law that allows diffraction pattern to be recorded in the film. However, we cannot directly change the incident beam direction. Rotating the samples in different directions is used instead.

There are three ways in sample rotation- around x-axis, around y-axis, and around z-axis. In this thesis, the counterclockwise orientation is treated as positive direction. A plan view showing how the sample around z-axial rotate (+)16° as follow.

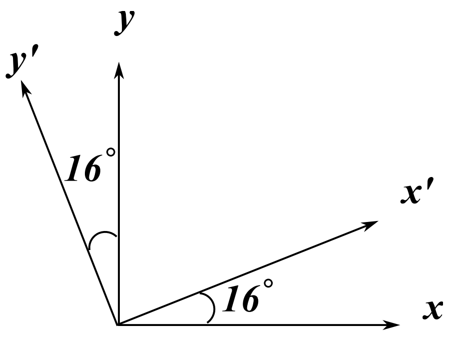

Figure 3-9 A sketch showing rotation around z-axial rotate (+)16°

In this situation, the $\mathbf{S_0}$= (-cos16°, sin16°, 0)

After all the information required calculating the $\mathbf{S_h}$ is obtained, another factor, the position of line directions of l_1 and l_2 in real crystal needs to be resolved.

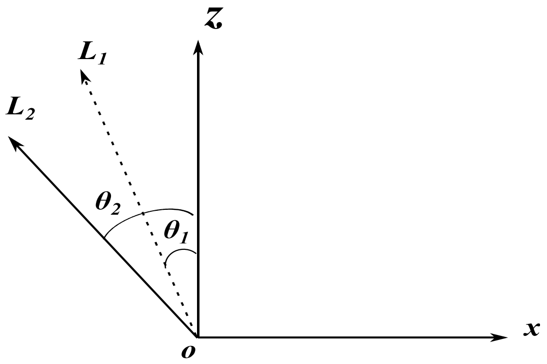

Figure 3-10 The way to measure the angle between dislocation direction and reference direction

First, from 2D image $\mathbf{l_1}$= ($-L_1\sin\theta_1$, 0, $L_1\cos\theta_1$), $\mathbf{l_2}$= ($-L_2\sin\theta_1$, 0, $L_2\cos\theta_2$).

In 3D situation, we need to use a combination of two matrices to express.

In a right-handed Cartesian coordinate system, a vector **L** can be rotated based on different axes in the 3D space. In a general case, a vector **L** becomes **L'** after rotation around the axis of x, y, and z with angle α, β and γ (Tait-Bryan angle) in a counter-clockwise direction, respectively. The direction of **L'** after the rotations of x, y, and z can be represented as:

$$\vec{\mathbf{L}}' = R_x(\alpha)\cdot R_y(\beta)\cdot R_z(\gamma)\vec{\mathbf{L}}$$

Here $R_x(\alpha), R_y(\beta), R_z(\gamma)$ are rotation matrices as follow:

$$R_x(\alpha) = \begin{pmatrix} 1 & 0 & 0 \\ 0 & cos\alpha & sin\alpha \\ 0 & -sin\alpha & cos\alpha \end{pmatrix} \tag{21}$$

$$R_y(\beta) = \begin{pmatrix} cos\beta & 0 & -sin\beta \\ 0 & 1 & 0 \\ sin\beta & 0 & cos\beta \end{pmatrix} \tag{22}$$

$$R_z(\gamma) = \begin{pmatrix} cos\gamma & -sin\gamma & 0 \\ sin\gamma & cos\gamma & 0 \\ 0 & 0 & 1 \end{pmatrix} \tag{23}$$

3.3 Experimental and results

The experiment was performed at the Advanced Photon Source (Beamline:1BM) in Argonne National Laboratory. The synchrotron sources can provide high resolution, wide wavelength range (0.2-2 A for white beam) and large X-ray area which can be up to 10 cm width and 1cm height. The crystal was mounted in transmission geometry. The film as a detector can be rotated in both horizontal and vertical plane to better record the diffraction pattern. Sample-film distance is usually set at 30cm. The typical exposure time is 30s which is adjustable decided by the storage ring current.

Several axial of 4H-SiC wafers were characterized. As a better illustration for the dislocation calculation process, a detailed information and calculation procedure will be given in the first place.

(1) Sample 1: An axial slice of 4H-SiC wafer ASQ (thickness: 350um)

- Surface plane: (11-20)
- Rotation angle and corresponding reflection: around z-axial rotate 16 °(counterclose) with (1-100) diffraction pattern; around y-axial rotate 10° (counterclose) with (0004) diffraction pattern
- The angle between dislocation line L and reference line: 4° for L1 and 1.7° for L2.

The diffraction images are shown in figure 3-11.

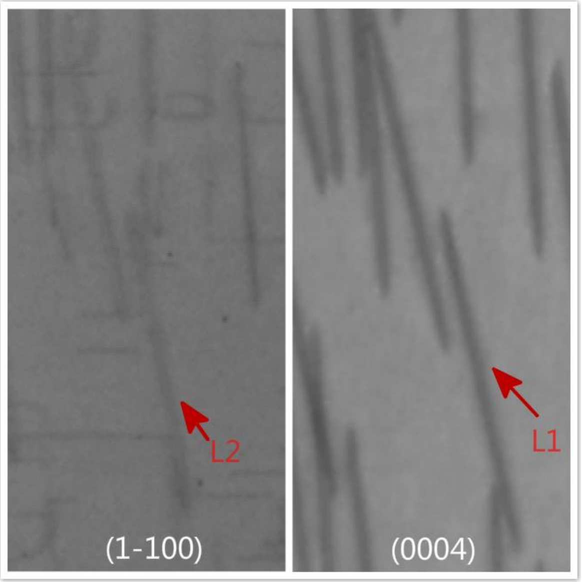

Figure 3-11 X-ray topographs recorded from axial SiC wafer within particular dislocation line of interest (L_1 and L_2)

Using Equation (8) (9) (10), the plane normal **g** for l_1= [001], for l_2= [0-10]

From the information of sample rotation,

$\mathbf{S}_{01}$= [-cos10°, 0, -sin10°], $\mathbf{S}_{02}$= [-cos16°, sin16°,0]

In Equation (3),

$$\begin{cases} -\vec{\mathbf{S_{0_1}}}\cdot\vec{\mathbf{g}} = sin10^\circ \\ \vec{\mathbf{S_{h_1}}}\cdot\vec{\mathbf{g}} = z \end{cases}$$

$$\Rightarrow \qquad z = sin10^\circ \qquad ,$$

In Equation (4),

$$\begin{cases} -\vec{\mathbf{S_{0_1}}}\times\vec{\mathbf{g}} = \begin{vmatrix} i & j & k \\ -cos10^\circ & 0 & -sin10^\circ \\ 0 & 0 & 1 \end{vmatrix} = 0\vec{i}+cos10^\circ\vec{j}+0\vec{k} = (0,cos10^\circ,0) \\ \vec{\mathbf{S_{h_1}}}\times\vec{\mathbf{g}} = \begin{vmatrix} i & j & k \\ x & y & sin10^\circ \\ 0 & 0 & 1 \end{vmatrix} = y\vec{i}-x\vec{j}+0\vec{k} = (y,-x,0) \end{cases}$$

$$\Rightarrow \qquad y = 0, x = -cos10^\circ$$

In conclusion,

$$\vec{\mathbf{S_{h_1}}} = (-cos10^\circ, 0, sin10^\circ)$$

Then, according to Equation (21) (22) (23),

$$\begin{cases} x = & -cos4^\circ sin10^\circ \\ y = & -sin4^\circ \\ z = & cos4^\circ sin10^\circ \end{cases}$$

$$\vec{L_1} = (-0.732, -0.0698, 0.9824)$$

Finally,

$$\begin{aligned} \vec{\mathbf{n_1}} &= \vec{\mathbf{S_{h_1}}}\times\vec{\mathbf{L_1}} \\ &= \begin{vmatrix} i & j & k \\ -cos10^\circ & 0 & sin10^\circ \\ -cos4^\circ sin10^\circ & -sin4^\circ & cos4^\circ cos10^\circ \end{vmatrix} \\ &= sin4^\circ sin10^\circ\vec{i} + (-sin^2 10^\circ cos4^\circ + cos4^\circ cos^2 10^\circ)\vec{j} + (cos10^\circ sin4^\circ)\vec{k} \\ &= (sin4^\circ sin10^\circ, -sin^2 10^\circ cos4^\circ + cos4^\circ cos^2 10^\circ, cos10^\circ sin4^\circ) \\ &= (0.0121, 0.9374, 0.0687) \end{aligned} \qquad .$$

Similarly, for L_2,

$$\vec{\mathbf{S_{h_2}}} = (-cos16^\circ, -sin6^\circ, 0)$$

$$\begin{aligned}\vec{\mathbf{L_2}} &= (-sin1.7^\circ sin16^\circ, -sin1.7^\circ cos16^\circ, cos1.7^\circ)\\ &= (-0.0082, -0.0285, 0.9996)\end{aligned}$$

Hence,

$$\begin{aligned}\vec{\mathbf{n_2}} &= \vec{\mathbf{S_{h_2}}} \times \vec{\mathbf{L_2}}\\ &= \begin{vmatrix} i & j & k \\ -cos16^\circ & sin16^\circ & 0 \\ -sin1.7^\circ sin16^\circ & -sin1.7^\circ cos16^\circ & cos1^\circ.7 \end{vmatrix}\\ &= -sin16^\circ sin1.7^\circ \vec{i} + (cos16^\circ cos1.7^\circ)\vec{j} + (sin1.7^\circ cos^2 16^\circ - sin1.7^\circ sin^2 16^\circ)\vec{k}\\ &= (-sin16^\circ sin1.7^\circ, cos16^\circ cos1.7^\circ, sin1.7^\circ(cos^2 16^\circ - sin^2 16^\circ))\\ &= (-0.02755, 0.9608, 0.0252)\end{aligned}$$

Finally, the dislocation line L direction is determined by

$$\begin{aligned}\vec{\mathbf{l}} &= \vec{\mathbf{n_1}} \times \vec{\mathbf{n_2}}\\ &= \begin{vmatrix} i & j & k \\ 0.0121 & 0.9374 & 0.0687 \\ -0.2755 & 0.9608 & 0.0252 \end{vmatrix}\\ &= (-0.0424, 0.0192, 0.2699)\\ &\xrightarrow{normalization} (-0.1549, -0.0702, 0.9854)\end{aligned}$$

This value is very close to **l**= (0, 0, 1), which means the direction of the chosen dislocation line is almost along [0001] direction in Hexagonal system. The observed result is shown in Figure 3-12 (a), which is consistent with the calculated result; the dislocation line in the real crystal is visualized in Figure 3-12 (b).

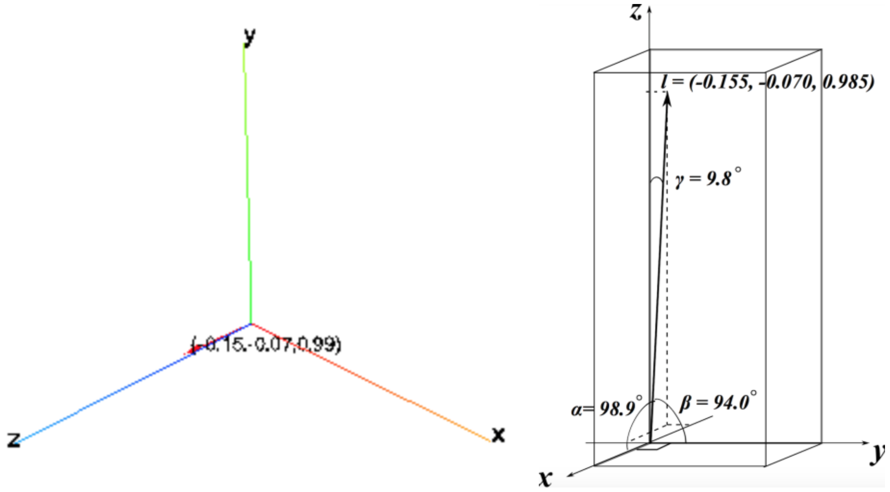

Figure 3-12 (a) The simulation result of dislocation line direction; (b) Visualized line direction in real crystal

(2) Sample 2: A 4H-SiC axial slice named LA (thickness: 354um)

- Surface plane: (11-20)
- Rotation angle and corresponding reflection: around z-axis rotate 24° (counterclose) with (-1100) (11-20) (1-101) (1-10-1) diffraction pattern; around y-axis rotate 8° (counterclose) with (0004) diffraction pattern

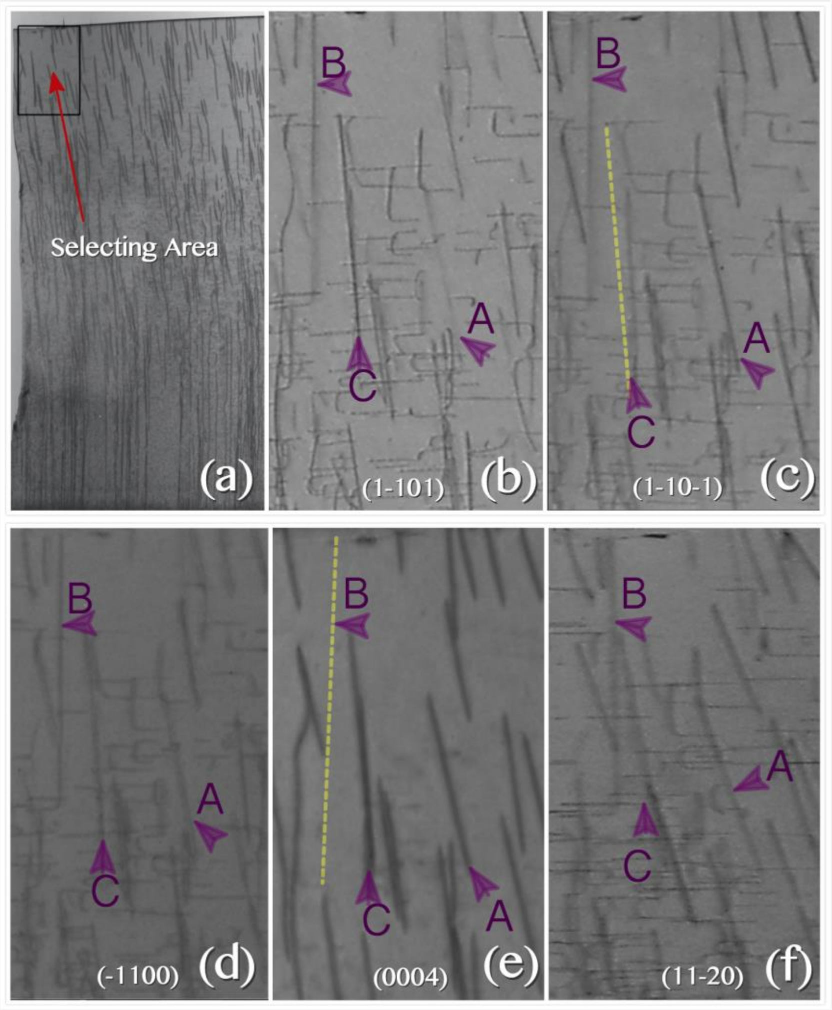

Figure 3-13 (a) 4H-SiC axial slice showing a certain area for axial wafer of LA; (b)-(f) The chosen area with different diffraction vectors: (1-101), (1-10-1), (-1100), (0004) and (11-20)

Figure 3-13 (a) shows the selected area from the sample 2. it is easy to tell these dislocations are growth-in dislocations as they nucleate in the seed and growth along the c-axis. Besides, most of these lines are long and straight, indicating they are threading dislocations. As introduced before, there are typically three categories of TDs, that is, threading edge dislocations (TEDs), threading screw dislocations (TSDs) and threading mixed dislocations (TMDs).

Figure 3-13 (b) to (f) show the same chosen area with different geometries, such as (-1100), (0004), (11-20), etc.

Similarly, line direction of a certain dislocation can be calculated. For example, dislocation A is in contrast on all the images. By choosing any two of them, the line direction of A can be calculated. Here we choose (0004) and (11-20) to do the calculation. Through the computer program, it is quickly to get the line direction of A is (0.0087, -0.0366, 0.9993), which is highly equals to [0001]. This means for this certain dislocation, it grows along c-axis.

However, more information is given from those diffraction images. For example, it is easy to find dislocation B disappears in (0004) spot, while dislocation C is out of contrast in (1-10-1) spot. Dislocation line direction information is not enough to explain these scenes. Hence, another important factor, Burgers vector is combined to help with the data analysis.

Based on dislocation theory and diffraction theory, the dislocation lines will be out of contrast if $\boldsymbol{g}.\boldsymbol{b}=\mathbf{0}$ is satisfied. Here, $\boldsymbol{g}$ is the reciprocal lattice vector associated with corresponding reflection and $\boldsymbol{b}$ is the Burgers vector of dislocations. This always works for screw-type dislocations. For edge-type or mix-type dislocations, another criterion needs to be satisfied. That is, $\boldsymbol{g}.\boldsymbol{b}\times\boldsymbol{l}=\mathbf{0}$, where $\boldsymbol{l}$ refers to dislocation line direction as mentioned in the above part.

Then, a $\mathbf{g}.\mathbf{b}$ analysis is conducted to analyze the dislocations (TSDs, TEDs, TMDs). The result is listed in Table 3-1.

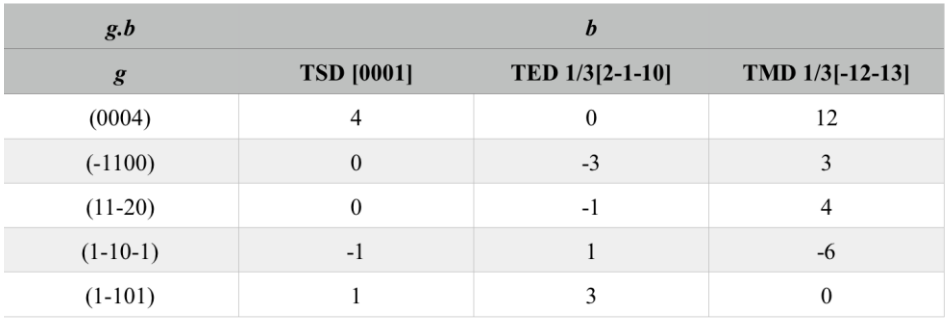

g.b	***b***		
g	**TSD [0001]**	**TED 1/3[2-1-10]**	**TMD 1/3[-12-13]**
(0004)	4	0	12
(-1100)	0	-3	3
(11-20)	0	-1	4
(1-10-1)	-1	1	-6
(1-101)	1	3	0

Table 3-1 Values of $\boldsymbol{g}.\boldsymbol{b}$ for TDs

Combined with $\boldsymbol{g}.\boldsymbol{b}=\mathbf{0}$ analysis, it indicates that dislocation B is threading edge dislocation as $\boldsymbol{g}.\boldsymbol{b}=\mathbf{0}$. Then, $\boldsymbol{g}.\boldsymbol{b}\times\boldsymbol{l}=\mathbf{0}$ analysis is necessary to define the category of dislocation B. Through calculation, the line direction of B is (-0.0010, -0.0023, -1.000), which is very close to [000-1]. It shows that dislocation B satisfies both $\boldsymbol{g}.\boldsymbol{b}=\mathbf{0}$ and $\boldsymbol{g}.\boldsymbol{b}\times\boldsymbol{l}=\mathbf{0}.$ Therefore, B is threading edge dislocation, which it is easy to glide through prismatic plane, such as (1-100), (-1100), etc.

For dislocation C, which is out of contrast in (1-10-1) spot, it highly suggests that this dislocation is a threading mixed dislocation with Burgers vector $\mathbf{nc}+\mathbf{ma}$ (m and n are integers). However, it is hard to measure the angle between dislocation line and reference line (c-axis) since two dislocation lines seems to cover each other. A good example of TMD analysis will be given in next part.

(3) Sample 3: A 4H-SiC axial slice named AQL (thickness: 350um)
- Surface plane: (11-20)
- Rotation angle and corresponding reflection: around z-axis rotate 18° (counterclose) with (1-100) (11-20) diffraction pattern; around y-axis rotate 6° (counterclose) with (0004) diffraction pattern

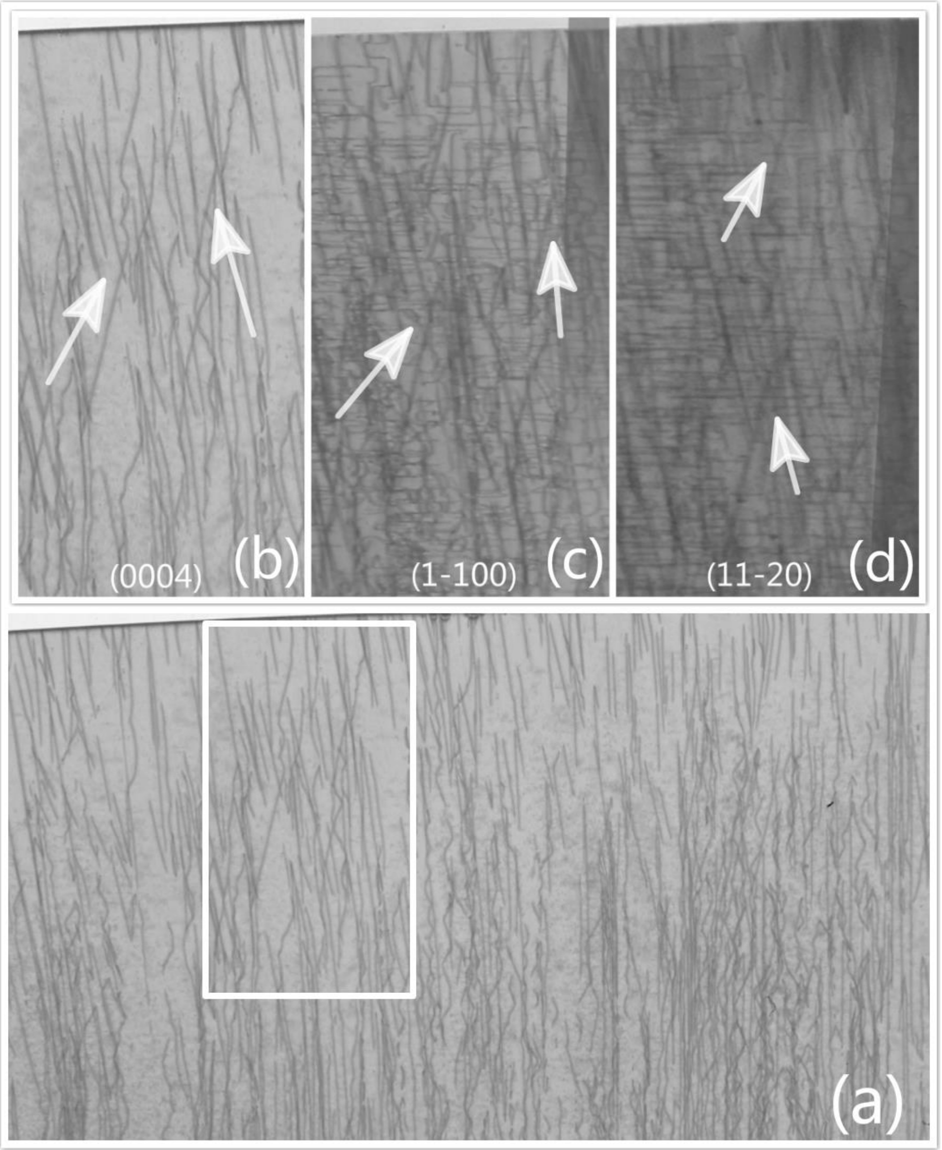

Figure 3-14 Threading mixed dislocation slide on plane (1-212)

Figure 3-14 (a) shows a part of the axial 4H-SiC wafer with numerous threading dislocations. While most of them grow along or slightly off-grow to axis, two dislocations, which particularly present high angle off-grow to axis, are of interest. As a large amount of threading dislocations are mixed dislocations with Burgers vector $\boldsymbol{nc}+\boldsymbol{ma}$ (m and n are integers) [45], plus the obvious glide trace on the image, it is predicable that this grown-in dislocation is under glide in certain slip system due to thermal stress.

Basically, the basal, prismatic and pyramidal slip systems are three common slip systems. For threading mixed dislocations, as the Burgers vector is along **nc + ma** (m and n are integers) direction, it is possible that this dislocation line glides on the pyramidal plane, as shown in Figure 3-15.

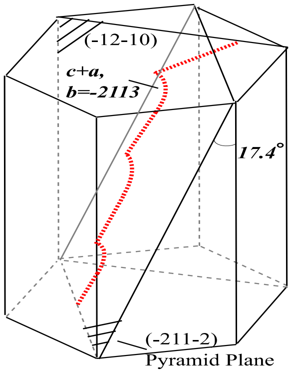

Figure 3-15 A sketch showing a dislocation glide on the pyramidal plane (-211-2)

It is well knowing that the combination of line direction and Burgers vector determine the preferential orientation for glide. To achieve this, we need to know the line direction of this dislocation first. Since the contrast on the third image is not good enough for analyzing, the (0004) and (1-100) planes were used to determine the line direction. The angle between dislocation line and reference line in (0004) spot is 20°, which is the same angle as the dislocation line and reference line in (1-100) spot. Note that the angle needs to be input as "-20°" when using the program because the tilt angle toward left is set as the positive direction.

Then, the calculation result is given by **l**= (-0.0768, -0.3596, -0.9299)

All the possible slip planes are listed below. The first order pyramidal planes are (10-11) (-1011) (1-101) (01-11) (-1101) (0-111), while the second order pyramidal planes are (11-22) (-1-122) (1-212) (-12-12) (2-112) (-2112). If **l** is in certain slip plane, it should satisfy **g.l=0**, when **g** stands for the normal of slip plane. Noted **l** works in a transformed-coordinate so it is necessary to transform **g** in the same manner. Equation (19) & (20) can be used in this situation.

From the calculation results, it shows that when the plane is (1-212), the normal of that plane is (-0.25, -0.43, 0.1532). The **g.l**= ((-0.0768x-0.25)+(-0.3596 x-0.43)+(0.1532x-0.9299))=0.03, which is almost equal to zero.

This means this dislocation line likely lies on (1-212) plane. Suppose the dislocation glides on this plane, another important factor needs to be satisfied. That is **b.g=0**, where **b** means the Burgers vector of threading mixed dislocations. For this type of dislocations, the Burgers vector could be 1/3[-2113], 1/3[-12-13], 1/3[-1-123], 1/3[2-1-13], 1/3[1-213], 1/3[11-23].

For **b**=1/3[-12-13], we have **b.g=0**, which means 1/3[-12-13] (1-212) is theoretically the slip system for this certain TMD. This study shows that dislocation line direction analysis can deduce tendency for dislocation glide and multiplication.

4. Summary

Conclusions

A method which can trace back the directions of the dislocations inside real crystals from two different dislocation X-ray topographic images, is developed and applied. The basic concept combines the crystal structure, rotation parameters and any two line-directions recorded on the X-ray film to determine the actual dislocation line direction in the real crystal. The hexagonal structure of 4H-SiC has been used to develop a computer program using JavaScript to perform this calculation. But the developed program can be easily modified to analyze dislocation line directions in any crystal structure. Application of the program using information from X-ray topographic images quickly produces quantitative results and also provides a graphical visualization of the 3D positions of dislocation lines inside 4H-SiC crystals. Especially, combined with Burgers vector data, this allows an effective way to analyze the formation mechanism and multiplication tendency of dislocations in crystals. Examples of this implementation are provided to demonstrate the significance of this procedure.

Future Work

This method can be further developed to incorporate additional geometries for recording X-ray topographs. The present method assumes that the film is placed parallel to the sample. To apply this to situations where the film is rotated with respect to the sample, a rotation matrix should be added. Further, the accuracy of measuring the angles between dislocation line and reference line (c-axis) on the diffraction image may be improved. The program could be modified to visualize orientation of dislocation line with respect to crystallographic axis.

References

[1] ROHM, www.rohm.com/us

[2] J. A. Cooper, Jr. and A. Agarwal, "SiC Power-Switching Devices-The Second Electronics Revolution," Proc.IEEE, vol. 90, no. 6, pp. 956-968, 2002.

[3] Shenai, Krishna, Michael Dudley, and Robert F. Davis. "Current status and emerging trends in wide bandgap (WBG) semiconductor power switching devices." ECS Journal of Solid State Science and Technology 2.8 (2013): N3055-N3063.

[4] Acheson A.G. (1892) English Patent No 17, 911.

[5] Lely J A 1955 Silicium, Schwefel, Phosphate, Colloq. Sek. Anorg. Chem. Intern. Union Reine u. Angew. Chem. (Munster) pp 20–4

[6] Tairov Y M and Tsvetkov V F 1978 J.Cryst.Growth 43 209–12

[7] Cree, www.cree.com

[8] Chaussende, D., P. J. Wellmann, and M. Pons. "Status of SiC bulk growth processes." Journal of Physics D: Applied Physics 40.20 (2007): 6150.

[9] Yakimova, Rositsa, and Erik Janzén. "Current status and advances in the growth of SiC." Diamond and related materials 9.3 (2000): 432-438.

[10] Selder, M., et al. "Numerical simulation of thermal stress formation during PVT-growth of SiC bulk crystals." Materials Science Forum. Vol. 353. 2001.

[11] Wagner, G., D. Schulz, and D. Siche. "Vapour phase growth of epitaxial silicon carbide layers." Progress in crystal growth and characterization of materials 47.2 (2003): 139-165.

[12] S. Nishino, J.A. Powell, H.A. Will, Appl. Phys. Lett. 42 (1983) 460.

[13] Song, Haizheng, M. V. S. Chandrashekhar, and Tangali S. Sudarshan. "Study of Surface Morphology, Impurity Incorporation and Defect Generation during Homoepitaxial Growth of 4H-SiC Using Dichlorosilane." ECS Journal of Solid State Science and Technology 4.3 (2015): P71-P76.

[14] Chandrashekhar, M. V. S., et al. "High purity semi-insulating 4H-SiC epitaxial layers by defect-competition epitaxy: controlling Si vacancies." Applied Physics Express 5.2 (2012): 025502.

[15] M. J. Loboda, G. Chung, E. Carlson, R. Drachev, D. Hansen, E. Sanchez, J. Wan and J. Zhang, “Advances in SiC substrates for power and energy applications,” in Proc. GOMACTECH Conference, 2011

[16] M. Dudley, S. Byrappa, H. Wang, F. Wu, Y. Zhang, B. Raghothamachar, G. Choi, E.K. Sanchez, D. Hansen, R. Drachev, M.J. Loboda, Materials Research Society Symposium Proceedings 1246 (2010) 29–34.

[17] Zulehner, Werner. "Historical overview of silicon crystal pulling development."Materials Science and Engineering: B 73.1 (2000): 7-15.

[18] Shenai, Krishna, et al. "(Invited) Crystal Defects in Wide Bandgap Semiconductors." ECS Transactions 61.4 (2014): 283-293.

[19] Klapper, Helmut. "Generation and propagation of defects during crystal growth." Springer handbook of crystal growth. Springer Berlin Heidelberg, 2010. 93-132.

[20] Dudley, M., et al., White beam synchrotron topographic analysis of multipolytype SiC device configurations. Journal of Physics D: Applied physics, 1995. 28: p. A56-A62.

[21] Huang, X. R., et al. "Direct evidence of micropipe-related pure superscrew dislocations in SiC." Applied physics letters 74.3 (1999): 353-355.

[22] Pernot, Etienne, et al. "Giant burgers vector micropipe-dislocations in silicon carbide investigated by atomic force microscopy." Materials science forum. Vol. 527. 2006.

[23] Zimmermann, U., et al., Investigation of microplasma breakdown in 4H SiC. Mater. Res. Soc. Symp. Proc, 1998. 512: p. 151-156.
[24] Loboda, M.J., et al., Advances in SiC Substrates for Power and Energy Applications. CS MANTECH Conference, 2011.

[25] Neudeck, P., H. Wei, and M. Dudley, Study of bulk and elementary screw dislocation assisted reverse breakdown in low-voltage (< 250 V) 4H-SiC pn junction diodes: DC properties. IEEE Trans. Electron. Dev., 1999. 46(3): p. 478-484.

[26] Wahab, Q., et al. "Influence of epitaxial growth and substrate-induced defects on the breakdown of 4H–SiC Schottky diodes." Applied Physics Letters 76.19 (2000): 2725-2727.

[27] Dudley, M., et al. "The mechanism of micropipe nucleation at inclusions in silicon carbide." Applied physics letters 75.6 (1999): 784-786.

[28] J. Takahashi, N. Ohtani, and M. Kanaya, J. Cryst. Growth 167, 596 1996.

[29] S. Ha, N. T. Nuhfer, G. S. Rohrer, M. De Graef, and M. Skowronski, J. Electron. Mater. 29, L5 2000.

[30] T.Ohno, H.Yamaguchi, S.Kuroda, K.Kojima, T.Suzuki, andK. Arai, "Direct observation of dislocation propagated from 4H-SiC substrate to epitaxial layer by X-ray topography" J.Cryst.Growth 260,p.209, 2004.

[31] S. Ha, P. Mieszkowski, M. Skowronski, and L. B. Rowland, J. Cryst. Growth 244, 257 2002.

[32] Ohno, T., et al. "Influence of growth conditions on basal plane dislocation in 4H-SiC epitaxial layer." Journal of crystal growth 271.1 (2004): 1-7.

[33] Chen, W. and M.A. Capano, Growth and characterization of 4H-SiC epilayers on substrates with different off-cut angles. Journal of Applied Physics, 2005. 98(11): p. 114907.

[34] Sudarshan, Tangali S., Haizheng Song, and Tawhid Rana. "Pretreatment Method for Reduction and/or Elimination of Basal Plane Dislocations Close to Epilayer/Substrate Interface in Growth of SiC Epitaxial Films." U.S. Patent Application No. 14/557,907.

[35] Dudley, M., et al. "Current Status of the Quality of 4H-SiC Substrates and Epilayers for Power Device Applications." MRS Advances 1.02 (2016): 91-102.

[36] J. Matthews and A. Blakeslee, Journal of Crystal Growth 27, 118 (1974).

[37] R. E. Stahlbush, K. X. Liu, Q. Zhang, and J. J. Sumakeris; Whole-wafer mapping of dislocations in 4H-SiC epitaxy; Mater. Sci. Forum 556–557, 295 (2007).

[38] Hansen, D., et al., Defect Reduction in SiC Growth Using Physical Vapor Transport. MRS Proceedings, 2010. 1246.

[39] Wang, H., et al. "Basal plane dislocation multiplication via the Hopping Frank-Read source mechanism in 4H-SiC." Applied Physics Letters 100.17 (2012): 172105.

[40] Wang, Huan Huan, et al. "Basal Plane Dislocation Multiplication via the Hopping Frank-Read Source Mechanism and Observations of Prismatic Glide in 4H-SiC." Materials Science Forum. Vol. 717. 2012.

[41] Tanner, Brian K. Characterization of crystal growth defects by X-ray methods. Vol. 63. Springer Science & Business Media, 2013.

[42] Autin, Bruno, et al. "The acceleration and storage of radioactive ions for a neutrino factory." Journal of Physics G: Nuclear and Particle Physics 29.8 (2003): 1785.

[43] J. H. Kinney et al., MRS Bulletin, (1988), Jau, 13

[44] H. P. Myers (2002).Introductory Solid State Physics. Taylor & Francis.ISBN 0-7484-0660-3

[45] F. Wu, H. Wang, S. Byrappa, B. Raghothamachar, M. Dudley, E. K. Sanchez, D. Hansen, R. Drachev, S. G. Mueller, and M. J. Loboda, Mater. Sci. Forum, 717-720, 343(2011).

[46] Yuan, Ding, and Michael Dudley. "Dislocation line direction determination in pyrene single crystals." Molecular Crystals and Liquid Crystals 211.1 (1992): 51-58.

Appendix: Code of Program

```
Main.html
<!DOCTYPE html>
<html>
<head>
    <title>drawing vector with three.js</title>
    <meta charset="utf-8">
    <meta name="viewport" content="width=device-width, user-scalable=no, minimum-scale=1.0, maximum-scale=1.0">
    <script type="text/javascript" src="three.min.js"></script>
    <script src="helvetiker_regular.typeface.js"></script>
    <script type="text/javascript" src="TrackballControls.js"></script>
    <script type="text/javascript" src="Detector.js"></script>
    <link rel="stylesheet" href="http://maxcdn.bootstrapcdn.com/bootstrap/3.2.0/css/bootstrap.min.css">
    <link rel="stylesheet" href="style.css">
</head>

<body>
    <div class="col-lg-12 col-md-12">
        <div class="col-lg-8">
            <div class="panel panel-default">
                <div class="panel-heading">
                    <h4>Crystal Structure </h4>
                <div class="row">
                    <div class="col-xs-2">
                        a
                        <input id="a" class="form-control" value="3.0806">
                    </div>
                    <div class="col-xs-2">
                        b
                        <input id="b" class="form-control" value="3.0806">
                    </div>
                    <div class="col-xs-2">
                        c
                        <input id="c" class="form-control" value="10.05">
                    </div>
                    <div class="col-xs-2">
                        alpha
                        <input id="alpha" class="form-control" value="90">
                    </div>
                    <div class="col-xs-2">
                        beta
                        <input id="beta" class="form-control" value="90">
```

```
            </div>
            <div class="col-xs-2">
                gamma
                <input id="gamma" class="form-control" value="120">
            </div>
        </div>
        <input type="checkbox" id="hcp"> HCP
    </div>
        <div class="panel-heading">
            <h4>Geometry 1 </h4>
        <div class="row">
            <div class="col-xs-2">x rotation<input id="x1" class="form-control" value="0">
            </div>
            <div class="col-xs-2">y rotation
                <input id="y1" class="form-control" value="0">
            </div>
            <div class="col-xs-2">z rotation
                <input id="z1" class="form-control" value="16">
            </div>
            <div class="col-xs-2">
                h
                <input id="h1" class="form-control" value="0"></div>
            <div class="col-xs-2">k
                <input id="k1" class="form-control" value="1"></div>
            <div class="col-xs-2">
                l
                <input id="l1" class="form-control" value="0"></div><p>
            <div class="col-xs-2">line rotation
                <input id="line1" class="form-control" value="1.7">
            </div>
        </div>
        </div>
        <div class="panel-heading">
            <h4>Geometry 2</h4>
        <div class="row">
            <div class="col-xs-2">x rotation
                <input id="x2" class="form-control" value="0">
            </div>
            <div class="col-xs-2">y rotation
                <input id="y2" class="form-control" value="0">
            </div>
            <div class="col-xs-2">z rotation
                <input id="z2" class="form-control" value="16">
            </div>
            <div class="col-xs-2">h
                <input id="h2" class="form-control" value="0">
```

```
                    </div>
                    <div class="col-xs-2">k
                        <input id="k2" class="form-control" value="1">
                    </div>
                    <div class="col-xs-2">l
                        <input id="l2" class="form-control" value="0">
                    </div>
                    <div class="col-xs-2">
                        line rotation
                        <input id="line2" class="form-control" value="12.4">
                        </div>
                </div>
                    <p>
                        <div class="panel-heading">
                            <button type="button" class="btn btn-success"
onclick="myFunction()">Update</button>
                        </div>
                </div>
            </div>
        </div>
        <div class="col-lg-4">
            <div class="panel panel-default">
                <div class="panel-heading">
                    <p id="s"></p>
                    <p id="g"></p>
                    <p id="sh"></p>
                    <p id="lh"></p>
                    <p id="n"></p>
                    <p id="demo"></p>
                    <canvas id='canvas'  style=" background-color: #ffffff" width="600"
height="350"></canvas>
                </div>
            </div>
        </div>
    </div>
    <script type="text/javascript" src="main.js"></script>
</body>
```

Main.js:

```
var a, b, c, alpha, beta, gamma;
var hkl1 = new Array(3),
    hkl2 = new Array(3);
var inverseG = new Array(9);
var g1 = new Array(3),
    g2 = new Array(3);
var h1 = new Array(3),
    h2 = new Array(3);
var s1, s2, l1, l2, n1, n2;
var l3;
var textStyle = {
            size: 4,
            height: 1,
            curveSegments: 1,
            font: "helvetiker",
            style: "normal"
        };
var textMaterial = new THREE.MeshBasicMaterial({
        color: 0x000000
    });

var renderer,
    scene = null,
    camera = null,
    controls = null,
    meshMaterial;
myFunction();

function getS(h, g) {
    var s = []
    var ip = h[0] * g[0] + h[1] * g[1] + h[2] * g[2];
    if (ip > 0) {
        for (var i = 0; i < 3; i++) {
            g[i] = -g[i];
        }
        ip = -ip;
    }
    for (var i = 0; i < 3; i++) {
        s.push(h[i] - 2 * ip * g[i]);
    }
    return s;
}

function getL(radians, radian) {
    var l = [];
    l.push(-Math.cos(radian) * Math.sin(-radians[1]));
```

```
    l.push(-Math.sin(radian));
    l.push(Math.cos(radian) * Math.cos(-radians[1]));
    return l;
}

function crossproduct(u, v) {
    var w = [];
    w.push(u[1] * v[2] - u[2] * v[1]);
    w.push(u[2] * v[0] - u[0] * v[2]);
    w.push(u[0] * v[1] - u[1] * v[0]);
    return w;
}

function rotateX(v, radians) {
    v[0] = v[0];
    v[1] = Math.cos(radians) * v[1] - Math.sin(radians) * v[2];
    v[2] = Math.sin(radians) * v[1] + Math.cos(radians) * v[2];
}

function rotateY(v, radians) {
    v[0] = Math.cos(radians) * v[0] + Math.sin(radians) * v[2];
    v[1] = v[1];
    v[2] = -Math.sin(radians) * v[0] + Math.cos(radians) * v[2];
}

function rotateZ(v, radians) {
    v[0] = Math.cos(radians) * v[0] - Math.sin(radians) * v[1];
    v[1] = Math.sin(radians) * v[0] + Math.cos(radians) * v[1];
    v[2] = v[2];
}
function getHKL(hkl, hcp, index){
    var h = (Number(document.getElementById("h"+index).value));
    var k = (Number(document.getElementById("k"+index).value));
    if(hcp){
        hkl[0] = h+k;
        hkl[1] = (k - h)/Math.sqrt(3);
    }else{
        hkl[0] = h;
        hkl[1] = k;
    }
    hkl[2] = (Number(document.getElementById("l"+index).value));
}

function myFunction() {
    a = Number(document.getElementById("a").value);
    b = Number(document.getElementById("b").value);
```

```
    c = Number(document.getElementById("c").value);
    alpha = Number(document.getElementById("alpha").value) / 180 * Math.PI;
    beta = Number(document.getElementById("beta").value) / 180 * Math.PI;
    gamma = Number(document.getElementById("beta").value) / 180 * Math.PI;

    var radians1 = new Array(3),
        radians2 = new Array(3);
    radians1[0] = (-Number(document.getElementById("x1").value) / 180 * Math.PI);
    radians1[1] = (-Number(document.getElementById("y1").value) / 180 * Math.PI);
    radians1[2] = (-Number(document.getElementById("z1").value) / 180 * Math.PI);
    radians2[0] = (-Number(document.getElementById("x2").value) / 180 * Math.PI);
    radians2[1] = (-Number(document.getElementById("y2").value) / 180 * Math.PI);
    radians2[2] = (-Number(document.getElementById("z2").value) / 180 * Math.PI);
    var radian1 = Number(document.getElementById("line1").value) / 180 * Math.PI;
    var radian2 = Number(document.getElementById("line2").value) / 180 * Math.PI;

    getHKL(hkl1, document.getElementById("hcp").checked, 1);
    getHKL(hkl2, document.getElementById("hcp").checked, 2);

    var cosalpha = Math.cos(alpha);
    var cosbeta = Math.cos(beta);
    var cosgamma = Math.cos(gamma);
    var sinalpha = Math.sin(alpha);
    var sinbeta = Math.sin(beta);
    var singamma = Math.sin(gamma);
    var m = 1.0 / (1 - cosalpha * cosalpha - cosbeta * cosbeta - cosgamma * cosgamma + 2 *
cosalpha * cosbeta * cosgamma);
    inverseG[0] = (sinalpha * sinalpha / a / a);
    inverseG[1] = ((cosalpha * cosbeta - cosgamma) / a / b);
    inverseG[2] = ((cosalpha * cosgamma - cosbeta) / a / c);
    inverseG[3] = ((cosalpha * cosbeta - cosgamma) / a / b);
    inverseG[4] = (sinbeta * sinbeta / b / b);
    inverseG[5] = ((cosbeta * cosgamma - cosalpha) / b / c);
    inverseG[6] = ((cosalpha * cosgamma - cosbeta) / a / c);
    inverseG[7] = ((cosbeta * cosgamma - cosalpha) / b / c);
    inverseG[8] = (singamma * singamma / c / c);
    console.log(inverseG);
    console.log(m);
    for (var i = 0; i < 3; i++) {
        var v1 = 0,
            v2 = 0;
        for (var j = 0; j < 3; j++) {
            v1 += m * inverseG[i * 3 + j] * hkl1[j];
            v2 += m * inverseG[i * 3 + j] * hkl2[j];
        }
        g1[i] = (v1);
```

```
        g2[i] = (v2);
      }
    normalize(g1);
    normalize(g2);
    h1[0] = (-1);
    h1[1] = (0);
    h1[2] = (0);

    h2[0] = (-1);
    h2[1] = (0);
    h2[2] = (0);
    rotateX(h1, radians1[0]);
    rotateY(h1, radians1[1]);
    rotateZ(h1, radians1[2]);
    rotateX(h2, radians2[0]);
    rotateY(h2, radians2[1]);
    rotateZ(h2, radians2[2]);

    s1 = getS(h1, g1);
    s2 = getS(h2, g2);

    l1 = getL(radians1, radian1);
    l2 = getL(radians2, radian2);

    var n1 = crossproduct(s1, l1);
    var n2 = crossproduct(s2, l2);
    l3 = crossproduct(n1, n2);
    normalize(l3);

    render();
    var round = 4;
    document.getElementById("s").innerHTML = "s1=(" + h1[0].toFixed(round) + ", " +
h1[1].toFixed(round) + ", " + h1[2].toFixed(round) + ")  <p> s2=(" + h2[0].toFixed(round) + ", "
+ h2[1].toFixed(round) + ", " + h2[2].toFixed(round) + ")";
    document.getElementById("g").innerHTML = "g1=(" + g1[0].toFixed(round) + ", " +
g1[1].toFixed(round) + ", " + g1[2].toFixed(round) + ") <p> g2=(" + g2[0].toFixed(round) + ", "
+ g2[1].toFixed(round) + ", " + g2[2].toFixed(round) + ")";
    document.getElementById("sh").innerHTML = "sh1=(" + s1[0].toFixed(round) + ", " +
s1[1].toFixed(round) + ", " + s1[2].toFixed(round) + ") <p> sh2=(" + s2[0].toFixed(round) + ", "
+ s2[1].toFixed(round) + ", " + s2[2].toFixed(round) + ")";
    document.getElementById("lh").innerHTML = "l1=(" + l1[0].toFixed(round) + ", " +
l1[1].toFixed(round) + ", " + l1[2].toFixed(round) + ") <p> l2=(" + l2[0].toFixed(round) + ", " +
l2[1].toFixed(round) + ", " + l2[2].toFixed(round) + ")";
    document.getElementById("n").innerHTML = "n1=(" + n1[0].toFixed(round) + ", " +
n1[1].toFixed(round) + ", " + n1[2].toFixed(round) + ") <p> n2=(" + n2[0].toFixed(round) + ", "
+ n2[1].toFixed(round) + ", " + n2[2].toFixed(round) + ")";
```

```
    document.getElementById("demo").innerHTML = "l=(" + l3[0].toFixed(round) + ", " +
l3[1].toFixed(round) + ", " + l3[2].toFixed(round) + ")";
}

function normalize(v) {
    var sum = 0;
    for (var i = 0; i < 3; i++) {
        sum += v[i] * v[i];
    }
    sum = Math.sqrt(sum);
    for (var i = 0; i < 3; i++) {
        v[i] /= sum;
    }
}


function render() {
    this.projector = null;

    if (!Detector.webgl) Detector.addGetWebGLMessage();
    var canvas = document.getElementById('canvas');
    renderer = new THREE.WebGLRenderer({
        canvas: canvas
    });

    canvas.width = canvas.clientWidth;
    canvas.height = canvas.clientHeight;
    renderer.setViewport(0, 0, canvas.clientWidth, canvas.clientHeight);
    renderer.setClearColorHex(0xeeeeee, 1.0);
    renderer.autoClear = false;
    document.body.appendChild(renderer.domElement);

    scene = new THREE.Scene();
    // Add some objects to the scene, one per quadrant
    /*meshMaterial = new THREE.MeshBasicMaterial({ color: 0xFF00FF, wireframe: true });

    var cube = new THREE.Mesh( new THREE.CubeGeometry( 5, 5, 5 ), meshMaterial );
    cube.position.set( 25, 25, 25 );
    scene.add( cube );

    var sphere = new THREE.Mesh( new THREE.SphereGeometry( 5 ), meshMaterial );
    sphere.position.set( -25, 25, 25 );
    scene.add( sphere );*/
```

```
    // We need a camera to look at the scene!
    camera = new THREE.PerspectiveCamera(45, canvas.width / canvas.height, 1, 10000);
    camera.position.set(120, 120, 120);
    camera.lookAt(scene.position);

    // And some sort of controls to move around
    // We'll use one of THREE's provided control classes for simplicity
    controls = new THREE.TrackballControls(camera, canvas);
    controls.rotateSpeed = 1.0;
    controls.zoomSpeed = 0.2;
    controls.panSpeed = 0.8;

    controls.noZoom = false;
    controls.noPan = false;

    controls.staticMoving = true;
    controls.dynamicDampingFactor = 0.3;

    drawAxes();
    drawVector();

    // and go!
    animate();
}

function drawAxes() {
    // Add axes
    axes = new THREE.AxisHelper(75) //buildAxes(1000);
    scene.add(axes);
    var textGeo = new Array(3);
    var text = new Array(3);
    var labels = ["x", "y", "z"];
    for (var i = 0; i < 3; i++) {
        textGeo[i] = new THREE.TextGeometry(labels[i], textStyle);

        text[i] = new THREE.Mesh(textGeo[i], textMaterial);
        text[i].position.x = axes.geometry.vertices[2*i+1].x;
        text[i].position.y = axes.geometry.vertices[2*i+1].y;
        text[i].position.z = axes.geometry.vertices[2*i+1].z;
        text[i].rotation = camera.rotation;
        scene.add(text[i]);
    }
}
function drawVector(){

    var dir = new THREE.Vector3(l3[0], l3[1], l3[2]);
```

```
   var origin = new THREE.Vector3(0, 0, 0);
   var length = 20;

   var arrowHelper = new THREE.ArrowHelper(dir, origin, length, 0xff0000);
   scene.add(arrowHelper);

   var  textGeo = new
THREE.TextGeometry("("+l3[0].toFixed(2)+","+l3[1].toFixed(2)+","+l3[2].toFixed(2)+")",
textStyle);
   var  text = new THREE.Mesh(textGeo , textMaterial);
   text.position.x = dir.x * length;
   text.position.y = dir.y * length;
   text.position.z = dir.z * length;
   text.rotation = camera.rotation;
   scene.add(text);
   console.log(arrowHelper.line.geometry.vertices)
}

function animate() {
   requestAnimationFrame(animate);
   controls.update();
   renderer.render(scene, camera);
}

function buildAxes(length) {
   var axes = new THREE.Object3D();

   axes.add(buildAxis(new THREE.Vector3(0, 0, 0), new THREE.Vector3(length, 0, 0),
0xFF0000, false)); // +X
   axes.add(buildAxis(new THREE.Vector3(0, 0, 0), new THREE.Vector3(-length, 0, 0),
0xFF0000, true)); // -X
   axes.add(buildAxis(new THREE.Vector3(0, 0, 0), new THREE.Vector3(0, length, 0),
0x00FF00, false)); // +Y
   axes.add(buildAxis(new THREE.Vector3(0, 0, 0), new THREE.Vector3(0, -length, 0),
0x00FF00, true)); // -Y
   axes.add(buildAxis(new THREE.Vector3(0, 0, 0), new THREE.Vector3(0, 0, length),
0x0000FF, false)); // +Z
   axes.add(buildAxis(new THREE.Vector3(0, 0, 0), new THREE.Vector3(0, 0, -length),
0x0000FF, true)); // -Z

   return axes;
}

function buildAxis(src, dst, colorHex, dashed) {
   var geom = new THREE.Geometry(),
      mat;
```

```
    if (dashed) {
        mat = new THREE.LineDashedMaterial({
            linewidth: 3,
            color: colorHex,
            dashSize: 3,
            gapSize: 3
        });
    } else {
        mat = new THREE.LineBasicMaterial({
            linewidth: 3,
            color: colorHex
        });
    }

    geom.vertices.push(src.clone());
    geom.vertices.push(dst.clone());
    geom.computeLineDistances(); // This one is SUPER important, otherwise dashed lines will appear as simple plain lines

    var axis = new THREE.Line(geom, mat, THREE.LinePieces);

    return axis;
}

Style.css:
```

```
/* Bootstrap Overrides */

.table>thead>tr>th, .table>tbody>tr>th, .table>tfoot>tr>th, .table>thead>tr>td, .table>tbody>tr>t
d, .table>tfoot>tr>td {
	vertical-align: middle;
}

/* Helper Classes */

.align-center  {
	text-align: center;
}

.align-left  {
	text-align: left;
}

.align-right  {
	text-align: right;
}

.bump-20	{
	margin-top: 20px;
}

.dimmed		{
	color: #ddd;
}

.padding-10  {
	padding: 10px;
}

.white-text  {
	color: #fff;
}

.label-player8 {
	background-color: #e469bf;
	color: #fff;
}

.axis path,
.axis line {
	fill: none;
	stroke: black;
```

```
            shape-rendering: crispEdges;
}

.axis text {
            font-size: 10px;
            font-family: sans-serif;
}

.area {
  fill: steelblue;
  opacity: 0.1;
}

.text-label {
            font-size: 10px;
            font-family: sans-serif;
}

table {
            text-align: center;
            border-collapse: collapse;
    border: 2px black solid;
    font: 12px sans-serif;
}
td, th {
            text-align: center;
            border: 1px black solid;
            padding: 5px;
}
th {
            text-align: center;
            font-weight: bold;
}

h6 {
            color: #722f37;
}

.fixed::before {
    content: "";
}
.btn-file {
    position: relative;
    overflow: hidden;
}
.btn-file input[type=file] {
```

```
    position: absolute;
    top: 0;
    right: 0;
    min-width: 100%;
    min-height: 100%;
    font-size: 100px;
    text-align: right;
    filter: alpha(opacity=0);
    opacity: 0;
    outline: none;
    background: white;
    cursor: inherit;
    display: block;
}
```